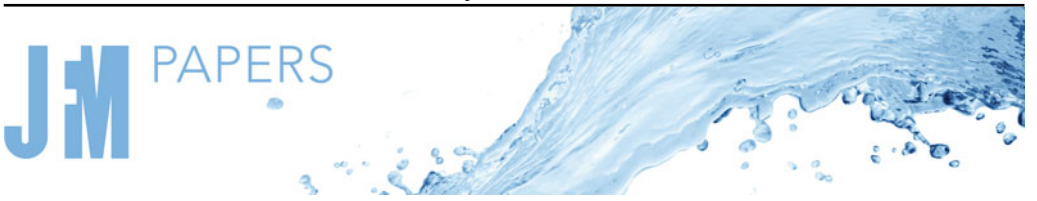
J. Fluid Mech. (2026), *vol.* 1037, A34, doi:10.1017/jfm.2026.11625



Genetic-algorithm-based control of a turbulent boundary layer

Jianing Yu[1,2] **and Yu Zhou**[1]

[1]School of Mechanical Engineering & Mechanics, Eastern Institute of Technology, Ningbo 315000, PR China

[2]Center for Turbulence Control, Harbin Institute of Technology, Shenzhen 315000, PR China

Corresponding author: Yu Zhou, yuzhou@eitech.edu.cn

(Received 1 June 2025 UTC; revised 9 April 2026 UTC; accepted 13 April 2026 UTC)

This work aims to investigate experimentally the control of a turbulent boundary layer over a flat plate based on a genetic-algorithm (GA)-based control system. A novel actuator is developed in house, consisting of one array of 11 spanwise-aligned synthetic minijets through longitudinal miniature slits, each independently controlled in terms of its exit momentum coefficient C_μ, frequency f_e and phase φ, while nine wall wires are placed downstream of the actuator to measure a variation in wall friction. A GA is employed for the unsupervised learning of near-optimal control strategies, i.e. the optimal φ of the synthetic jets, with f_e and C_μ optimized first. The learning process unveils three typical control strategies that may attain substantial drag reduction (DR) in both actuation and downstream regions, i.e. conventional uniform forcing (CUF), GA-I and GA-II. The latter two are characterized by the triangle- and trapezoid-like distributions of φ, respectively, thus each producing a spanwise motion. The three strategies achieve spanwise-averaged local DR by 45 %, 52 % and 52 %, respectively. The downstream drag-reducing areas exhibit an appreciable difference between the three cases, with CUF recovering drag more rapidly than the other two. It has been found that the three cases are associated with different DR mechanisms and flow physics, which account for the distinct control performances.

Key words: turbulent boundary layers, drag reduction, machine learning

1. Introduction

Interest in the friction drag reduction (DR) of a turbulent boundary layer (TBL) has been constantly increasing in the past few decades due to its potential benefits in numerous engineering applications. Skin friction drag is closely connected to quasistreamwise

© The Author(s), 2026. Published by Cambridge University Press.

https://doi.org/10.1017/jfm.2026.11625 Published online by Cambridge University Press

vortices (QSVs). These structures take place largely in the buffer layer, which is immediately above the large wall shear stress (WSS) sublayer (Kravchenko, Choi & Moin 1993; Orlandi & Jiménez 1994). The dynamics of these QSVs is directly responsible for the generation of Reynolds shear stress and hence viscous drag. The well-known events, i.e. sweeps and ejections, streaky structures, are all associated with the QSVs (e.g. Kim 1983; Hussain 1986). For example, the low-speed streaks result from the ejection process on the upwash side of the QSVs, whilst the high-speed streaks are formed on the downwash side (Kline *et al.* 1967). The latter contributes to large skin friction events (Jeong *et al.* 1997). The streaks are unstable to the normal mode instability (Hamilton, Kim & Waleffe 1995) and even more so to the non-normal mode instability (Schoppa & Hussain 2002), giving rise to the streamwise-dependent disturbance and thus the generation of the new QSVs. The inflectional instability is associated with the lifted flows, which accounts for the occurrence of bursts, the major source of turbulence production (Kline *et al.* 1967).

The TBL control techniques can be passive or active. Passive techniques, involving no energy input, include riblets (e.g. Walsh 1983; Choi, Moin & Kim 1993), miniature vortex generators (Zhang *et al.* 2023), compliant (e.g. Lee, Fisher & Schwarz 1993; Choi *et al.* 1997; Fukagata *et al.* 2008) and superhydrophobic surfaces (e.g. Daniello, Waterhouse & Rothstein 2009; Martell, Perot & Rothstein 2009; Alamé & Mahesh 2019), etc. These techniques are characterized by permanent fixtures, unable to adapt to varying working conditions. For example, riblets and compliant surfaces suffer from less-efficient DR when flow conditions (e.g. Reynolds number) change, while the performance of superhydrophobic surfaces deteriorates easily in practical environments (Checco *et al.* 2014; Rastegari & Akhavan 2018). In contrast, active control has the potential to achieve more flexible and drastic flow modifications. Naturally, many active methods have been proposed and investigated with success to different degrees, such as wall oscillation, wall deformation, introducing large-scale streamwise vortices (LSSVs) and blowing or suction, etc. The in-plane wall oscillation is extensively investigated both numerically (e.g. Jung, Mangiavacchi & Akhavan 1992; Quadrio & Ricco 2004; Quadrio, Ricco & Viotti 2009; Skote 2011) and experimentally (e.g. Choi & Clayton 2001; Di Cicca *et al.* 2002). This technique may achieve a DR of approximately 40 % (Quadrio 2011). The wall-normal deformation is another technique. A standing-wave-like wall deformation alone does not result in any significant DR (Mito & Kasagi 1998). However, as demonstrated by Endo, Kasagi & Suzuki 's (2000) and Kang & Choi's (2000) direct numerical simulation (DNS) in a turbulent channel flow, this technique may achieve a DR of 10 %–17 % when combined with a feedback control. The wall-normal deformation may also form a spanwise travelling wave, and the experimental (Itoh *et al.* 2006; Li *et al.* 2018) and numerical (Tomiyama & Fukagata 2013) studies of this technique demonstrated a DR of 4 %–13 % in TBLs or turbulent channel flow. The streamwise travelling-wave-like wall deformation seems more effective based on the DNS data, achieving a DR of 69 % with a net energy saving of 65 % (Nakanishi, Mamori & Fukagata 2012) at a low Reynolds number based on u_τ ($Re_\tau = 180$). This DR technique is, however, less effective when Re_τ increases say beyond 1500 based on the scaling analysis by Nabae, Kawai & Fukagata (2020). One drawback associated with the wall deformation or oscillating motion is the difficulty in implementing such techniques in engineering. Introducing artificially LSSVs is another effective method to achieve DR, as demonstrated numerically by Schoppa & Hussain (1998) and experimentally by Iuso *et al.* (2003) at a low Reynolds number. Using externally generated LSSVs, Canton *et al.* (2016*a*,*b*) achieved numerically in a turbulent channel flow a DR of 18 % at $Re_\tau = 180$ but no DR once Re_τ was raised to 550. In their DNS studies,

https://doi.org/10.1017/jfm.2026.11625 Published online by Cambridge University Press

Yao *et al.* (2017, 2018) chose correctly the height of an externally generated wall jet and obtained a DR of 12 % at $Re_\tau = 550$. Wong *et al.* (2015), Corke & Thomas (2018), Thomas *et al.* (2019), Duong, Corke & Thomas (2021), Cheng *et al.* (2021*b*) and Wei & Zhou (2024, 2025) developed experimentally plasma actuators for the generation of the LSSVs, achieving substantial DRs, up to 78 %, in TBLs.

Blowing and suction have also been rather extensively studied both experimentally and numerically for the DR of TBLs. It is now well established that steady blowing may reduce the skin friction, accompanied by a rapid decrease in turbulence intensity near the wall but an increase farther away from the wall, which is related to the uplifted streamwise vortices (Park & Choi 1999; Kametani & Fukagata 2011). On the other hand, suction does the opposite (Park & Choi 1999; Kim, Kim & Sung 2003). However, the skin friction farther downstream of the control area shows the opposite, i.e. an increase in the blowing case and a decrease in the suction case, which is ascribed to the flow destabilization and stabilization by blowing and suction, respectively, as observed by Antonia, Zhu & Sokolov (1995) in a TBL control experiment when suction was done through a short porous spanwise wall strip. In fact, given an adequately high suction rate, the pseudorelaminarization took place downstream of suction, leading to a DR of 50 %. Periodic blowing experimentally through a spanwise slot may result in a temporal relaminarization within 40 wall units downstream of the slot, achieving a local DR of 45 % but producing a drag increase of 200 % farther downstream (Tardu 2001). The periodic blowing through one array of streamwise slits may lead to a maximum DR of 70 % in the experiment, even with a net energy saving of 2.2 % (Cheng *et al.* 2021*a*).

Attention has also been given to TBL control via wall normal synthetic jets in the experiment, which can be generated through circular or rectangle orifices. Circular synthetic jets can achieve a local DR of 12 %–30 % downstream of the actuator (Spinosa & Zhong 2017; Lu *et al.* 2020). Rathnasingham & Breuer (2003) used three synthetic jets through streamwise slits to manipulate a TBL. The slits of 160 wall units (l_v) in length and 10 l_v in width were spanwise-separated by 40 l_v, where l_v is the wall unit. They reported a local maximum DR of 7 % downstream of the synthetic jets. Ye *et al.* (2019) used one array of synthetic jets through longer (400 l_v) and wider (26.7 l_v) slits, where the spanwise separation between slits was 560 l_v. The local DR reached 30 %. Yu *et al.* (2022) developed one array of six synthetic jets through smaller scale longitudinal slits, with 150 l_v in length, 6.7 l_v in width and a spanwise spacing of 20 l_v. They measured a maximum local DR of 48 % downstream of the slits.

Active control often involves more than one control parameter. Conventional open-loop control searches for optimal performance by manually adjusting individual control parameters which is time-consuming and inefficient. Closed-loop control may adjust the control parameters dynamically based on the feedback or feedforward information on the control target (Qiao, Zhou & Wu 2017). The proportional integral derivative and opposition controllers have demonstrated their effectiveness and efficiency in reducing skin friction of the TBL (Choi, Moin & Kim 1994; Abbassi *et al.* 2017; Qiao *et al.* 2017; Qiao, Wu & Zhou 2018). However, the closed-loop control may in general optimize only up to two or three control parameters (Wu, Wong & Zhou 2018; Fan, Zhou & Noack 2020*b*). A large number of control parameters or a large opportunity space is bound to contain more desirable solutions, and the associated optimal or near optimal solutions may exceed greatly that offered by the opportunity space of two or three control parameters. However, it is a challenge to find optimal control laws when many control parameters are involved.

https://doi.org/10.1017/jfm.2026.11625 Published online by Cambridge University Press

Machine learning or artificial intelligence (AI) control provides a powerful vehicle for optimizing active flow control. Various techniques based on different algorithms have been developed, including linear genetic programming (e.g. Gautier *et al.* 2015; Li *et al.* 2017), genetic algorithm (GA) (e.g. Minelli *et al.* 2020; Qiao *et al.* 2021; Yu *et al.* 2022), reinforcement learning (e.g. Rabault *et al.* 2019; Lai *et al.* 2021; Paris, Beneddine & Dandois 2021), explorative gradient method (EGM) (e.g. Fan *et al.* 2020*a*; Li *et al.* 2022) and ant colony optimization (Zhang *et al.* 2023*a*). Zhou *et al.* (2020) provided an excellent demonstration on how AI can find the optimum control strategies and provide new insight into the flow physics. They developed an AI control system based on linear genetic programming for enhancing a turbulent jet mixing using six independently operated distributed minijets as actuators, involving the optimization of 18 independent parameters. Their analysis of the proximity map or all the control strategies identified in the learning process unveiled four distinct flow structures, i.e. three classical forcings (axisymmetric forcing, helical forcing and flapping) and a highly complicated forcing never reported before. The new forcing is characterized by, *inter alia*, both swirling around an oscillating axis and three-dimensional (3-D) flapping, much more effective in enhancing mixing than those classical ones.

There is a scarcity of research on the machine-learning-based control of TBL due to a few challenges related to this highly complex flow, including how to capture reliably the friction force and how to manipulate the flow. The latter involves the difficulties in the development of actuator and controller. Yu *et al.* (2022) developed a GA-based evolutionary control system to manipulate a TBL. A maximum local DR of 48 % was obtained 33 l_v downstream of the synthetic jets. This very first attempt suffers from several limitations. Firstly, they used only six independently operated synthetic jets through longitudinal slits, covering an actuation width of only 100 l_v, corresponding to the average separation between low-speed streaky structures (Kline *et al.* 1967). Secondly, their investigation involved only six independent control variables, i.e. the initial phases of the synthetic jets. The search space is relatively small. Thirdly, the cost function consisted of local WSS from only two wall wires, implying locally targeted DR and giving no information on the spanwise averaged DR. Fourthly, they reported only the maximum DR and did not analyse the large amount of data generated during the learning process, thus missing possibly valuable information associated with the data. For example, how was the optimal solution found? Was there any alternative optimal solution? Finally, little information was given on how the flow structure altered under control and what the DR mechanisms were.

The purpose of this experimental work is to address the aforementioned issues. The manuscript is organized as follows: §§ 2 and 3 describe the experimental set-up and synthetic jet-induced flow, respectively. The control system and how it works are presented in § 4. The data-driven optimization process and the performances of representative optimized control laws or individuals are given in § 5. The modified flow structures and the mechanisms for DR are discussed in § 6. This work is concluded in § 7.

2. Experimental details

2.1. *Generation of fully developed TBL*

Experiments were carried out in a closed-loop wind tunnel, with a horizontal test section of 5.6 m in length, 0.8 m in width and 1.0 m in height, at The Center for Turbulence Control, Harbin Institute of Technology (Shenzhen). The rig to generate zero-pressure-gradient TBL is the same as Cheng *et al.* (2021*a*,*b*), thus not repeated here. Measurements

https://doi.org/10.1017/jfm.2026.11625 Published online by Cambridge University Press

U_∞ (ms^{-1})	δ_{99} (mm)	δ_1 (mm)	θ (mm)	H_{12}	Re_θ	Re_{δ_1}	Re_τ	u_τ (ms^{-1})	l_v (mm)	t_v (s)
2.4	85	13.1	9.2	1.41	1450	2044	572	0.105	0.15	0.0014

Table 1. Characteristic parameters of the uncontrolled TBL.

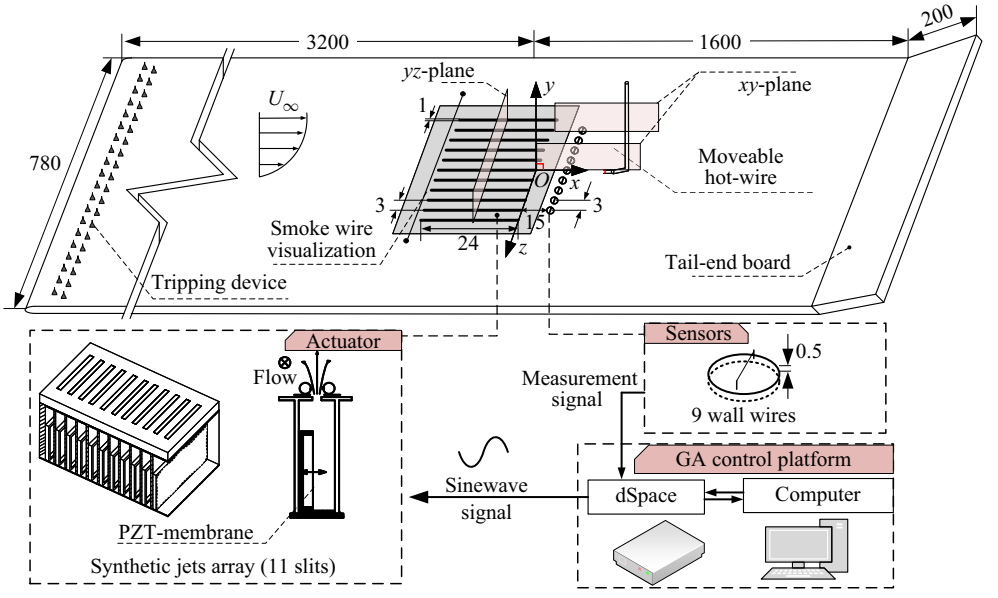


Figure 1. Schematic of the experimental set-up, including the actuator, its installation, the measurement and the workflow of data-driven optimization (not to scale; units in millimetres).

were conducted at a free stream velocity $U_\infty = 2.4\,\mathrm{ms}^{-1}$, and the corresponding free stream longitudinal turbulence level was 0.4 %. Table 1 lists the characteristic parameters of the uncontrolled TBL at the test position, 3.2 m downstream of the leading edge of the plate (figure 1), including the TBL thickness δ_{99}, momentum thickness θ, displacement thickness δ_1, shape factor $H_{12} = \delta_1/\theta$, friction velocity u_τ ($\equiv \sqrt{\overline{\tau_w}/\rho}$, where τ_w is the local WSS, ρ is the density of air and the overbar denotes time-averaging), $l_v = \nu/u_\tau$ (ν is the kinetic viscosity of air), time scale $t_v = l_v/u_\tau$, Reynolds number $Re_\theta = U_\infty\theta/\nu$, $Re_{\delta_1} = U_\infty\delta_1/\nu$ and $Re_\tau = u_\tau\delta_{99}/\nu$. Unless otherwise stated, the superscript '+' and '∗' in this paper denote normalization by the inner and outer scales in the absence of control, respectively. The coordinate system (x, y, z) is defined in figure 1, with its origin at the trailing edge and symmetry point of the synthetic minijet array. The instantaneous velocities along the x, y and z directions are denoted by $U = \overline{U} + u$, $V = \overline{V} + v$ and $W = \overline{W} + w$, respectively, where u, v and w are the fluctuating components.

2.2. *Actuator and control platform*

The actuator consists of one array of 11 synthetic jets through longitudinal slits, fabricated in-house and spanwise-arranged uniformly. The innovativeness of this actuator lies in the miniature size of the synthetic jets and furthermore each jet can be independently operated. Both features are crucially important for this investigation. Firstly, each slit has a width of $7l_v$ and a longitudinal length of $160l_v$, and the spanwise centre-to-centre

https://doi.org/10.1017/jfm.2026.11625 Published online by Cambridge University Press

separation between adjacent slits is $20l_v$, comparable to those ($3l_v$, $133l_v$ and $20l_v$) used by Cheng *et al.* (2021*a*). These dimensions are in the same order of magnitude as those of predominant coherent structures in the TBL (Jacobson & Reynolds 1998). For example, the QSVs feature with a length of approximately $200lv$ (Smith 1984) and the low-speed streaks are on average approximately $60l_v$ in width and $1000l_v$ in length, with a spanwise separation of $100l_v$ (Kline *et al.* 1967; Smith 1984). Secondly, as demonstrated by Zhou *et al.* (2020), AI may have great advantages over conventional control techniques only when involving many control variables, in general exceeding three, and its deployment may find new control strategies and mechanisms. Cheng *et al.*'s (2021*a*) minijets were synchronized since it would be extremely difficult, if not impossible, to make their minijets independently operated due to the very small spanwise centre-to-centre separation between adjacent slits and the bulky size of electromagnetic valves involved. However, the present innovative actuator overcomes this difficulty, each synthetic minijet being independently operated, thus with up to 33 independent control variables.

The synthetic minijet is generated by a vibrating piezoelectric (PZT) membrane of 30 mm × 20 mm × 0.2 mm (length × width × thickness). As shown in figure 1, this membrane is mounted vertically, with both ends fix-supported, in a chamber made of an aluminium alloy base. The separation between the membrane and the base wall is 0.7 mm, larger than the maximum oscillation amplitude of the membrane to avoid a clash. The thickness of the wall between two adjacent chambers is 1 mm. It has been confirmed that there is no interaction in terms of vibrations between two adjacent units. Every membrane is monitored in its capacitance, approximately 1 μF, during experiments to ensure its good working order. Driven by a sinusoidal signal, the oscillating membrane creates a synthetic jet through a longitudinal slit of 1 mm in width and 24 mm in length. The entire synthetic jet array occupies an area of 32 mm (spanwise) × 24 mm (streamwise) or 200 l_v × 160 l_v, and the spanwise separation of adjacent slits is 3 mm or 20 l_v. A synthetic jet S_i is driven by an independent sinusoidal signal $V_{t,i} = V_{0,i} \sin(2\pi f_i t + \phi_i)$, $i = 1, 2, \ldots, 11$, generated from the dSPACE control system (t is time). The peak voltage $V_{0,i}$ and frequency f_i can be any value in 0∼30 V and 200∼600 Hz, respectively. Beyond this frequency range, the PZT membrane may vibrate irregularly. Here ϕ_i is the initial phase, where ϕ_1 is set to zero to avoid reduplicated actuation strategies.

A real-time control platform dSPACE is deployed to process the input signals and output control signals based on the user-defined control logic. The outputs from the 16-bit digital-to-analogue converter of the platform are amplified by a dual channel piezo driver amplifier (Trek PZD 700) to drive the PZT membranes. All input and output signals are recorded synchronously at a sampling frequency of 5 kHz.

2.3. *Flow measurements*

A total of nine fixed wall wires and one movable hot-wire (Dantec 55P15) are used to measure the local WSS and the velocity profile in the TBL, respectively. The sensing element of each wire, made of tungsten, was 5 μm or 0.033 l_v in diameter and 1.2 mm or 8 l_v in length. The overheat ratio was set as 1.5 for all wires. The wires were operated on constant-temperature anemometers (Dantec Streamline). The signal from the wire was low-pass filtered at a cutoff frequency of 3 kHz and then sampled at 6 kHz using a 16-bit analogue-to-digital converter. The movable hot-wire was mounted on a 3-D traversing mechanism, with a spatial resolution of 3.125 μm in all three directions. The hot-wire is calibrated with a Pitot tube connected to a micromanometer (FCO510, with a resolution of 0.001 Pa). The WSS can be estimated by the slope of $\overline{U}$ profile in the viscous sublayer measured using the movable hot-wire, following, e.g. Hutchins & Choi (2002).

https://doi.org/10.1017/jfm.2026.11625 Published online by Cambridge University Press

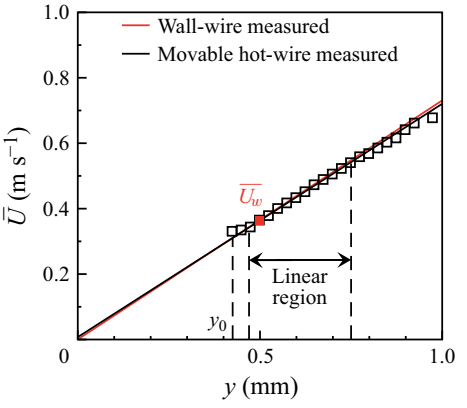


Figure 2. Comparison in the time-averaged streamwise velocity between the wall wire (■) and traversing hot-wire (□) measurements.

The profile consists of 26 points along the y direction with an increment of 0.025 mm, as illustrated in figure 2. The duration of each hot-wire signal was recorded for 40 s. Evidently, the data are well fitted to a linear curve, except for a couple of points near the wall deviating from the linear curve due to the wall effect (Hutchins & Choi 2002). As such, we may determine the wall position, and the distance y of the measurement point from the wall. Following Qiao, Xu & Zhou (2019), we used a total station theodolite to measure the position y_0 of the valid measurement point nearest to the wall. The maximum difference between two different estimates in y_0 is no more than 3 %. Then, the time-averaged WSS $\overline{\tau_w}$ can be calculated from $\overline{\tau_w} = \mu(\mathrm{d}\overline{U}/\mathrm{d}y)$, and five repeated measurements indicate an uncertainty of no more than 1.8 %.

Additional, nine wall-wires named $W_1 \sim W_9$ were placed at $x^+ = 100$ (figure 1), downstream of the second through 10th slit, respectively, to measure the local WSS or drag variation. The sensing element and supporting prongs are immersed in the TBL, producing a minimum disturbance to the flow. As in figure 2, the thermal effect of the wall could be felt at $y^+ < 3$ (Hutchins & Choi 2002). Therefore, the distance between wall-wire and the wall was 0.5 mm or 3.3 l_v. The calibration process for the wires is the same as Qiao *et al.* (2017). Because the wall wire was placed in the viscous layer or linear region whose thickness was approximately 0.75 mm, the WSS can also be calculated from $\overline{\tau_w} = \mu(\mathrm{d}\overline{U}/\mathrm{d}y) = \mu(\overline{U_w}/y)$, where $\overline{U_w}$ and y are the wall-wire-measured velocity, time-averaged over a duration of 40 s, and the wire distance from the wall. The accuracy of this method is slightly lower than the first method based on the slope of $\overline{U}$ in viscous layer, and the uncertainty of five repeated measurements is 3 %. This method is only used in the data-driven optimization process to reduce the cost of time. Once an optimal control strategy is identified, $\overline{\tau_w}$ will be remeasured using the first method. Subsequent $\overline{\tau_w}$ downstream of the actuation is also measured using the first method. The corresponding local time-averaged drag variation $\overline{\delta_{\tau_w}} = [(\overline{\tau_w})_{on} - (\overline{\tau_w})_{off}]/(\overline{\tau_w})_{off}$, where the subscripts 'on' and 'off' denote the values with and without control, respectively.

A Dantec particle image velocimetry (PIV) system was deployed to measure the TBL and the actuator-induced flow in different planes. The tracer particles with an average diameter of approximately 1μm were generated from olive oil by a particle generator (TSI 9307-6). A double-pulse laser system with a spherical lens and a cylindrical lens creates a laser sheet of 1 mm thickness. One charge-coupled device (CCD) camera was used to capture the images in the mode of double frames (2560 pixels × 1600 pixels). The image covers an area of 46 mm × 30 mm for measurements in the x–y planes of $z^+ = 0$ and –70

https://doi.org/10.1017/jfm.2026.11625 Published online by Cambridge University Press

or an area of 40 mm × 25 mm in the y–z plane of $x^+ = -80$. A total of 2700 image pairs were captured in each plane at a framing rate of 15 Hz. A low-frequency laser with the trigger frequency $f_t = 15$ Hz is unable to capture the full picture of the flow at the various phases of synthetic jets. However, given specific imaging frequencies, i.e. $kf_t + 1$ Hz (k is a positive integer), the CCD camera captures the first pair of images at $t = 0$ in the first cycle of the synthetic jets, the second and third pairs at $t = k(1/15)T$ and$k(2/15)T$, respectively, where T is the period of the synthetic jets. Then we may obtain 15 different phases of the synthetic jets. For instance, take $T = 0.002$ s, then the 15 Hz laser can only capture three phases of the synthetic jets but may capture 15 phases of the synthetic jets given $kf_t + 1 = 496$ Hz ($k = 33$). Therefore, in PIV experiments, we used the synthetic jets of 496 Hz instead of 500 Hz. It has been confirmed that mean velocity, vorticity, production and dissipation of turbulent kinetic energy (TKE) all converged to a maximum departure of 1 % once the number of images exceeds 2000 pairs.

The PIV system was also used for smoke-wire flow visualization in the x–z plane of $y^+ = 7$ in the TBL, though the double-pulsed laser was replaced by a continuous laser source. The smoke wire made of NiCr alloy with a diameter of 0.05 mm was placed at $y^+ = 5$, oriented parallel to the plate and perpendicular to incoming flow. A uniform smoke sheet is produced once the wire is heated by an adequately strong direct electric current. Here U_∞ is chosen to be 1.8 ms^{-1} to ensure high-quality flow visualization images. The imaging rate was 500 frames (120 mm × 75 mm) per second.

3. Natural TBL and synthetic jets

3.1. *The TBL in the absence of control*

It is important to ensure the generation of a fully developed TBL at the position where the measurements are conducted. The TBL in our work is fully developed, characterized by zero-pressure gradient. The Reynolds numbers, Re_θ and Re_{δ_1}, based on the momentum thickness and displacement thickness, respectively, with a shape factor of $H_{12} = 1.41$, which is very close to the reported results. The shape factor H_{12} Spalart (1988) measured is 1.43 at $Re_\theta = 1410$, and Cheng *et al.* (2021*a*,*b*) found $H_{12} = 1.41$ at $Re_\theta = 1450$. Pirozzoli & Smits (2023) summarized the characteristic properties of the zero-pressure gradient TBL ($Re_{\delta_1} = 10^3 \sim 10^5$) and showed that H_{12} gradually decreased from 1.5 to 1.2 with increasing Re_{δ_1}. At $Re_{\delta_1} = 2000$, H_{12} is approximately 1.42. The $\overline{U^+}$ and u^+_{rms} profiles of the baseline TBL collapse well with the published canonical TBL data, as shown in figure 3. Furthermore, these profiles measured at $z^+ = 0$ and ± 150 also exhibit a good collapse, suggesting a spanwise homogeneity.

3.2. *Characteristics of synthetic jets*

It is important to document the characteristics of the synthetic jets. A single hot-wire is placed parallel to the slit at $(x^+, y^+, z^+) = (-80, 3.3, 0)$ to measure the exit velocity ${U_{jet}}^+$ at the centre of the middle slit in the absence of incoming flow. Figure 4 illustrates the time histories of ${U_{jet}}^+$ and the input signal V_t of the PZT membrane. Note that a second minor peak in V_t results from the flow reversal associated with the synthetic jet. The lasting durations of blowing and suction, marked by the dashed and dotted lines, are identical. The peak of blowing is higher than that of suction, as noted by Utturkar *et al.* (2008) and Qayoum *et al.* (2010), largely due to a difference in the effective cross-sectional area at the jet exit between the two stages. The actuator is characterized via a delay in response time by 0.12 ms as shown in figure 4. Before experiments, the time delays of all synthetic

https://doi.org/10.1017/jfm.2026.11625 Published online by Cambridge University Press

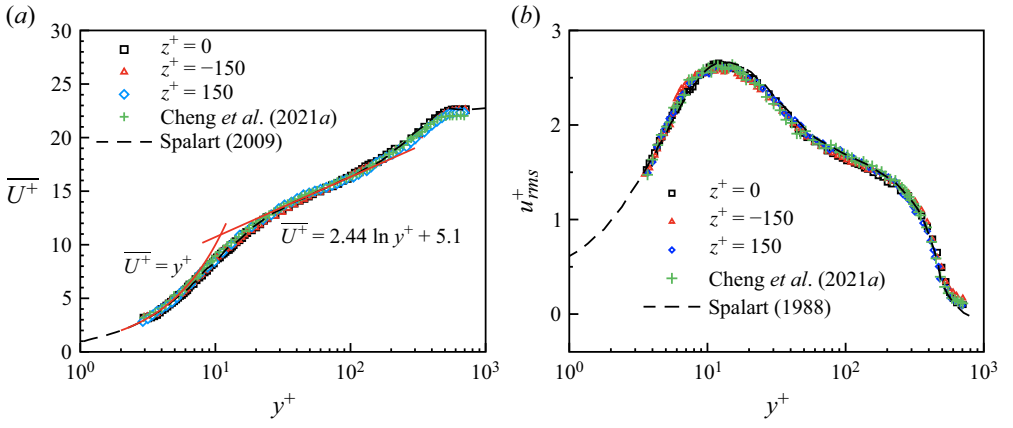


Figure 3. Distributions of (*a*) time-averaged streamwise velocity $\overline{U^+}$ and (*b*) r.m.s. value u^+_{rms} at three different spanwise locations ($x^+ = 33$, $z^+ = -150$, 0, 150) in the natural TBL.

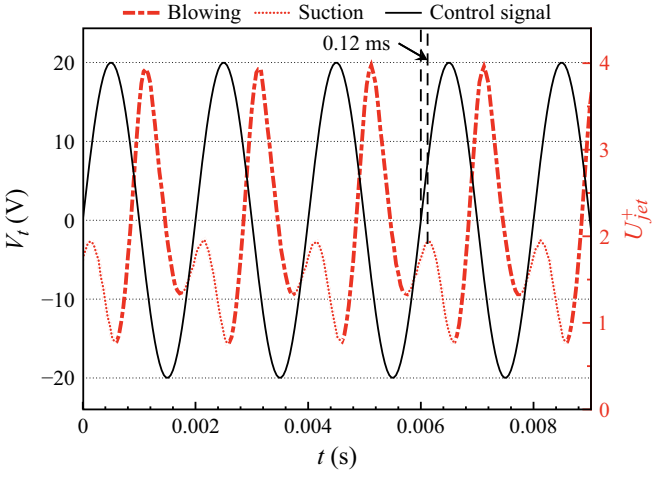


Figure 4. Control and typical velocity signals measured at (x^+, y^+, z^+) = (–80, 3.3, 0) using a hot-wire. The voltage on PZT membrane is 500 Hz and 40 V.

jets were measured and adjusted on the dSPACE control system to ensure that they were identical to each other.

4. Data-driven optimization

4.1. *Control system*

It is a challenge for conventional optimization methods to deal with a problem with a large number of variables where 33 independent parameters ($V_{0,i}$, f_i, φ_i, $i = 1, 2, \ldots, 11$) are involved with the 11 spatially distributed synthetic jets. It is the data-driven optimization that provides us with a means to find the optimal or near optimal solution to this problem. Our developed data-driven optimization system is schematically shown in figure 5. The system consists of the control plant (TBL), actuation unit (11 synthetic jets), sensing unit (nine wall wires) and control unit based on GA. The control plant, actuation unit and sensing unit have been discussed in §§ 2.1, 2.2 and 2.3, respectively. The control goal is

https://doi.org/10.1017/jfm.2026.11625 Published online by Cambridge University Press

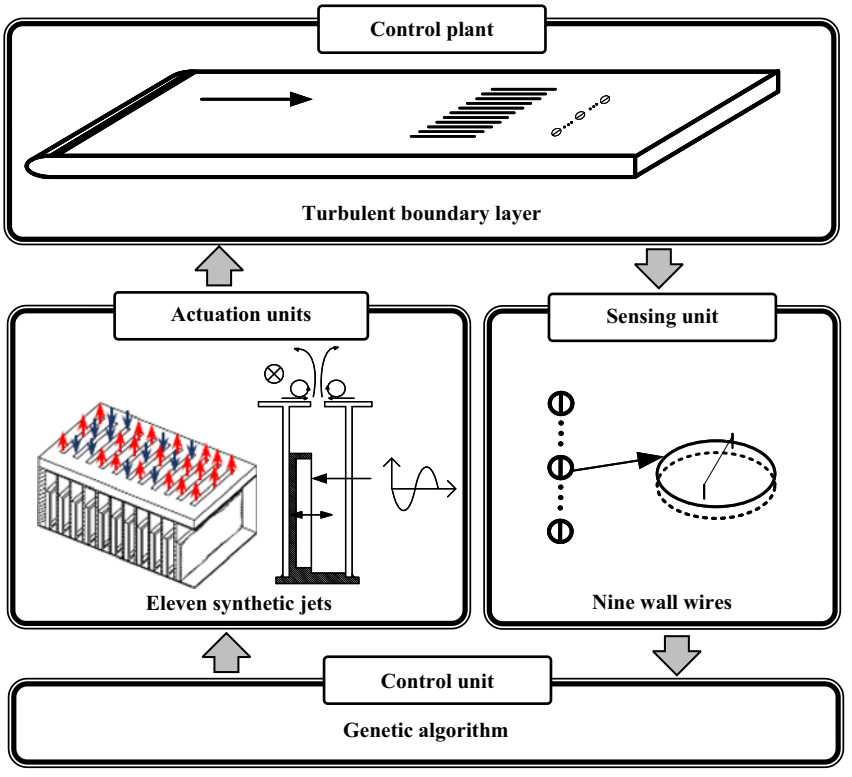


Figure 5. Workflow of data-driven optimization system.

to minimize the cost function J, defined as $J = 1 + (1/9)\sum_{i=1}^{9}\overline{\delta_{\tau_w,i}}$, where $\overline{\delta_{\tau_w,i}}$ is the time-averaged drag variation measured from the ith wall wire W_i. Thus, a minimized J corresponds to the maximum spanwise averaged DR at $x^+ = 100$.

The present choice of the GA is due to following considerations. First, the wall-wire-measured DR contains errors, which introduces noises in the estimation of the cost function. The GA is robust to such noises, thanks to the repeated crossover and re-evaluation of individual control strategies (e.g. Zhou *et al.* 2020). As such, this algorithm is commonly used in experiments targeting the optimization of flow control (e.g. Benard *et al.* 2016; Debien *et al.* 2016; Qiao *et al.* 2021; Zigunov, Sellappan & Alvi 2021). In contrast, the gradient-based methods heavily rely on the gradient information and are prone to being misled by experimental noises, even falling into local optima (Lou, Sun & Nocedal 2025). Second, the number of sensors presently optimized is limited, only nine, making it difficult to use methods like DRL that require a large number of sensors (Paris *et al.* 2021). For instance, Rabault *et al.* (2019) and Tang *et al.* (2020) used 151 and 236 probes, respectively, to control the two-dimensional wake of a cylinder. Finally, an algorithm must possess strong global search capabilities to handle the high nonlinearity of a TBL and a large sample space, involving presently more than 10 parameters. The GA has reached a relatively mature stage of development, and its widely recognized global search capability is particularly prominent when dealing with high-dimensional complex optimization problems (Brunton & Noack 2015). In our preliminary work, we compared the search performances of EGM (Li *et al.* 2022) and GA. The EGM combines the downhill simplex method for local extremum search and Latin hypercube sampling for global search. Although the EGM algorithm could discover better control

https://doi.org/10.1017/jfm.2026.11625 Published online by Cambridge University Press

strategies than conventional uniform forcing (CUF) and converge faster than GA, its converged result remained inferior to those of GA. Analysis of the search process or landscape reveals that, while the Latin hypercube sampling method exhibits a certain level of global search capabilities, its random search efficiency is excessively low for high-dimensional and complex sample spaces, leading to a premature convergence to local optima. Indeed, the GA may find control strategies that are completely out of our expectation and uncover new physical mechanisms of DR. In their jet-mixing optimization, Zhou *et al.* (2020) demonstrated that linear genetic programming, a GA-based algorithm, progressively identified the well-known jet-mixing mechanisms and eventually converged to a never reported highly effective jet-mixing mechanism. The TBL is a highly complex flow, compared with a turbulent jet. As such, we deployed in the first stage actuators with a search space as large as 33 parameters (synthetic jet frequency, exit momentum and phase). However, we failed to find any good control strategy (to be discussed later). This is because GA cannot get around the curse of dimensionality when dealing with very high-dimensional complex sample spaces; with increasing population sparsity, the algorithm tends to degenerate into a random search (Goldberg 1989). As such, we choose to optimize the excitation frequency and exit momentum first and then optimize the individual phases of the synthetic jets, thus reducing the search space to a maximum of 11 control parameters.

4.2. *Optimization based on GA*

The actuation commands are given by $\boldsymbol{V_t} = [V_{t,1}, V_{t,2}, \ldots, V_{t,11}]$, where $V_{t,i} = V_{0,i} \sin(2\pi f_i t + \varphi_i)$ is the actuation signal for the ith synthetic jet. Vectors $\boldsymbol{V_0} = [V_{0,1}, V_{0,2}, \ldots, V_{0,11}]$, $\boldsymbol{f} = [f_1, f_2, \ldots, f_{11}]$ and $\boldsymbol{\varphi} = [\varphi_1, \varphi_2, \ldots, \varphi_{11}]$ are considered to be optimized. A GA-based optimization searches for individuals,

$$\boldsymbol{K} = (\boldsymbol{V}_0, \boldsymbol{f}, \boldsymbol{\phi}) \tag{4.1}$$

so that the cost is minimized, and the optimal individuals is

$$\boldsymbol{K}^\star = \arg\min_{\boldsymbol{K}} J[\boldsymbol{K}]. \tag{4.2}$$

The first generation of GA contains $N_i = 100$ sets of rather randomly chosen control parameters, and each set is also referred to as an individual or control law. In the searching process of the data-driven optimization system (figure 5), every individual is tested for 40 s to estimate the corresponding cost function J_i^n, where the superscript n denotes the nth generation. There is a 5 s interval from the evaluation of one individual to another to minimize the interference between evaluations. Subsequent generations are produced from the previous one with genetic operations, i.e. elitism, crossover, mutation and replication, which will be discussed in detail later. Again, the evaluation of the individuals in new generation is the same as the previous generation. After the *in situ* performance evaluations, the individuals in each generation are renumbered in descending order, *viz.*

$$J_1^n \leqslant J_2^n \leqslant \ldots \leqslant J_{N_i}^n \, J_1^n \leqslant J_2^n \leqslant \ldots \leqslant J_{N_i}^n. \tag{4.3}$$

where the subscript i represents the individual index. The above processes are repeated until the cost functions are converged.

4.3. *Choices of GA parameters*

The choice of the GA parameters needs to take into account both convergence speed and optimization results. Elitism is a process that passes a given number of top-ranking individuals directly to the next generation, thus guaranteeing that the next generation

https://doi.org/10.1017/jfm.2026.11625 Published online by Cambridge University Press

Parameters	Value
Population size	$N_i = 100$
Elitism	$N_e = 3$
Tournament size	$N_t = 7$
Crossover	$P_c = 50\,\%$
Mutation	$P_m = 30\,\%$
Replication	$P_r = 20\,\%$

Table 2. Key parameters of GA.

will not perform worse than the previous one. The individuals of the next generation are selected via a tournament process. A certain number, determined by the tournament size N_t, of randomly chosen individuals, compete in a tournament and the winner is selected based on the value of J. Replication copies a statistically selected number of individuals into the next generation. Thus, some well-performing individuals are preserved. Crossover involves two statistically selected individuals from the tournament and generates a new pair of individuals, with part of their parameters swapped. This operation contributes to breeding better individuals by searching the space around well-performing individuals. The mutation operation, where the random parts of the statistically selected individuals are modified, serves to explore potentially new individuals with a smaller J. The parameters of GA in this study are given in table 2. Following Yu *et al.*'s (2021) preliminary work, the choice of the parameters was obtained after numerous trial-and-error tests. The number of top-ranking individuals is chosen to be $N_e = 3$ for elitism operation. The size for tournament is set as $N_t = 7$. The population size N_i of each generation is set as 100. There should be a compromise between reduced populations (approximately 50–500) and high mutation rates P_m (from 25 % to 50 %) to ensure diversity (Duriez, Brunton & Noack 2017). Therefore, P_m is set as 30 %. On the other hand, the crossover rate P_c influences the ability to global search and is generally higher than P_m (Duriez *et al.* 2017), thus being made 50 %. Finally, replication ensures the exploration of a given search space during a certain number of generations and its rate P_r is set as 20 % since $P_c + P_m + P_r = 1$.

Note that the choice of the GA parameters does have an impact upon the optimization performance. In almost all algorithms, including GA, the hyperparameters may affect the optimization performance. Tuning these parameters is always an important part of data-driven optimization. However, there are many references that document the choice of the parameters, especially for matured algorithms such as GA. The influence of each parameter is quite predictable on the search performance. Therefore, this disadvantage is acceptable as per the good results it may lead to.

4.4. *Control landscape*

Insight into the control landscape or overall picture and its evolution of control laws may be gained from proximity maps via multidimensional scaling (Cox & Cox 2000). The essence of this scaling is to ensure that the relative distances between the examined control laws or individuals are essentially unchanged after a high-dimensional space is mapped to a two-dimensional space $\boldsymbol{\gamma_i} = (\gamma_{i,1}, \gamma_{i,2})$. This method is employed in a number of investigations (e.g. Duriez *et al.* 2017; Zhou *et al.* 2020), to produce the proximity map of individuals.

https://doi.org/10.1017/jfm.2026.11625 Published online by Cambridge University Press

Its key is to find a feature vector $\boldsymbol{\gamma_i}$ so that

$$\sum_{i=1}^{N_i\times n}\sum_{j=1}^{N_i\times n}(||\boldsymbol{\gamma}_i-\boldsymbol{\gamma}_j||-D_{ij})^2=\min, \tag{4.4}$$

where the metric D_{ij} is the Euclidean distance between individuals $\boldsymbol{K_i}$ and $\boldsymbol{K_j}$, given by

$$D_{ij}=\left|\left|\boldsymbol{K}_i-\boldsymbol{K}_j\right|\right|\ (i,\ j=1,\ 2,\ \ldots,\ N_i\times n). \tag{4.5}$$

Finally, the proximity map may be constructed via interpolation based on the 3-D data points ($\gamma_{i,1}$, $\gamma_{i,2}$, J_i), $i=1,\ 2,\ \ldots,\ N_i\times n$. The feature vectors $\boldsymbol{\gamma}_i$ are connected by an unstructured grid $i1,i2,i3\in\{1,\ \ldots,\ Ni\times n\}$ from triangulation proposed by Delaunay (1934). The J values in each mesh triangle are interpolated from the known values at the vertices of each triangle J_{i1}, J_{i2}, J_{i3}. Zhang *et al.* (2023) and Zhou *et al.* (2020) have demonstrated that a careful analysis of the control landscape may unveil the characteristics of actuations and representative effective control strategies.

5. Performance of control

5.1. *Conventional uniform forcing*

The CUF is first investigated as a reference. Following the same procedures as Bai *et al.* (2014) and Yu *et al.* (2022), the optimal f^+ and $U^+{}_{jet,max}$ for the 11 synthetic jets are found to be 0.71 (500 Hz) and 4.0, respectively, and the resulting cost function J_{CUF} is 0.63. The dependence of $\overline{\delta_{\tau_w}}$, on x^+ and z^+ is presented in figure 6*a*. The $\overline{\delta_{\tau_w}}$ exhibits little spanwise variation, approximately –45 %, in the central region, over $z^+=-40\sim40$, downstream of synthetic jets $S_1\sim S_8$. From $z^+=40$–70 or –40 to –70, $\overline{\delta_{\tau_w}}$ drops until reaching its minimum, –55 %, at $z^+\approx\pm70$ and then gradually rises from $z^+=\pm80$ to ±100. As will be shown later, the occurrence of this minimum is due to the generation of a spanwise velocity $\overline{|W|}^+=2$ at $y^+=4$ near slits S_1 and S_{11}, which is induced by the asymmetric actuation around two slits. Such a spanwise velocity enhances the DR (Cheng *et al.* 2021*b*). The rise in $\overline{\delta_{\tau_w}}$ is ascribed to the 3-D effect. That is, the TBL is characterized by strong spanwise asymmetry resulting from the shear generated in the process where neighbouring elongated high- or low-speed regions interact through a localized spanwise motion as propagating downstream (Johansson, Alfredsson & Kim 1991). Under the influence of the near-wall meandering high- and low-speed streaky structures, the fluid near the edge of the controlled region quickly resumes to their uncontrolled state due to the entrainment of fluid motions unaffected by control.

The spanwise-averaged DR is 45 %, doubling that achieved at the same x^+ by Bai *et al.* (2014) who used one array of cantilever-supported PZT actuators. Like Cheng *et al.*'s (2021*a*) unsteady jets blowing through longitudinal slits, the synthetic jets are characterized by longer effective longitudinal length and their drag-reducing effect persists much farther downstream than that produced using cantilever-supported PZT actuators. As shown in figure 6(*b*), $\overline{\delta_{\tau_w}}$ rises rather rapidly from –45 % at $x^+=33$ to –10 % at $x^+=300$ and then slowly to zero at $x^+=500$ without overshooting. Bai *et al.* (2014) obtained a local DR of approximately 50 % at $x^+=17$, which fully recovered at $x^+=160$. Other than the influence of the effective actuation length, the injection of zero-streamwise-momentum (ZSM) fluid into the TBL is beneficial to the DR (Kametani & Fukagata 2011). Note that the periodic blowing through an array of streamwise slits by Cheng *et al.* (2021*a*) achieved a maximum DR up to 77 % at $x^+=33$, but the WSS recovers gradually to the natural state at $x^+\approx500$, followed by an overshoot.

https://doi.org/10.1017/jfm.2026.11625 Published online by Cambridge University Press

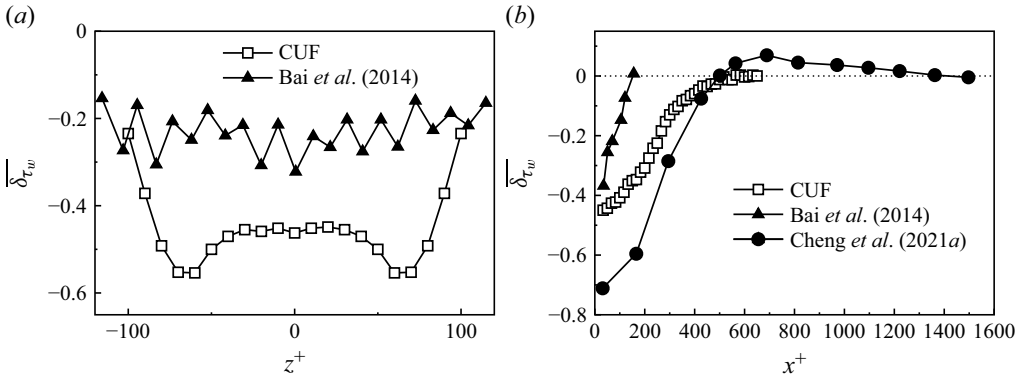


Figure 6. (*a*) Spanwise variation of local DR $\overline{\delta_{\tau_w}}$ measured at $x^+ = 33$, (*b*) longitudinal variation of $\overline{\delta_{\tau_w}}$ measured at $z^+ = 0$. Control parameters: $U^+{}_{jet,max} = 4, f^+ = 0.71$.

The presently observed DR does not persists very far, compared with Schoppa & Hussain (1998) report based on the DNS data obtained in a turbulent channel flow. When their LSSVs suddenly disappears, the DR effect is appreciable even at $x^+ = 16\,000$. They quantified this distance by $\Delta x \approx U_c{}^+ \Delta t^+$, where $U_c{}^+ = 16$ is the normalized centreline velocity of the channel flow, thus leading to their statement of the low drag state persisting downstream at least 16 000 wall units. This estimate assumes that the convection velocity of the controlled flow is advected at $U_c{}^+$. However, the convection velocity of controlled flow, especially in the viscous sublayer, is much smaller than $U_c{}^+$. In the experimental studies of TBL controlled by LSSVs, the DR does not persist that far as Schoppa & Hussain's (1998) report. In their experimental investigation, Iuso *et al.* (2002) deployed high-speed wall jet, approximately $100u_\tau$, to generate LSSVs in a turbulent channel flow and observed a complete disappearance of DR at 9000 wall units downstream of the actuator. Cheng *et al.* (2021*b*) produced experimentally a maximum spanwise jet velocity of only $4u_\tau$ using plasma actuators to generate LSSVs and observed a DR of only 2000 wall units. The present synthetic jets produce smaller scale disturbances. It would then not be surprising to see that the DR persists only of the order of 500 wall units, as also noted by Rathnasingham & Breuer (2003), Kim & Sung (2006) and Cheng *et al.* (2021*a*).

The difference in $\overline{\delta_{\tau_w}}$ at $x^+ = 33$ between synthetic jets and blowing jets may suggest that the averaged DRs over the control area differ between the two techniques. Xi, Quadrio & Zhou (2024) performed the DNS of a turbulent channel flow manipulated using steady and unsteady blowing through one array of longitudinal slits with the same geometric configuration as Cheng *et al.* (2021*a*). Their results under unsteady blowing agree quite well with Cheng *et al.*'s (2021*a*) data in terms of streamwise variations in the DR, mean energy dissipation rate and production downstream of actuation. They observed an averaged DR of 57 % over the control area and a small variation in $\overline{\delta_{\tau_w}}$, from 70 % to 60 %, over $x^+ = 10 \sim 100$. Their finding confirms that the large DR observed downstream of the blowing jets results from the substantial DR in the control area. It may be inferred from the DR measured at $x^+ = 33$ that the actuation of the present synthetic jet array may have produced substantial averaged DR over the control area, albeit less than the blowing jet array. It may not be surprising to see that the synthetic jets are not so effective as blowing jets. There is a difference in the DR mechanisms between the two techniques. While preventing sweep events from reaching the wall, the blowing jets inject ZSM fluid into the near-wall region. The low-momentum fluids spread and result in decelerated flow, largely near the wall, and hence relaminarization (Cheng *et al.* 2021*a*). However, the

https://doi.org/10.1017/jfm.2026.11625 Published online by Cambridge University Press

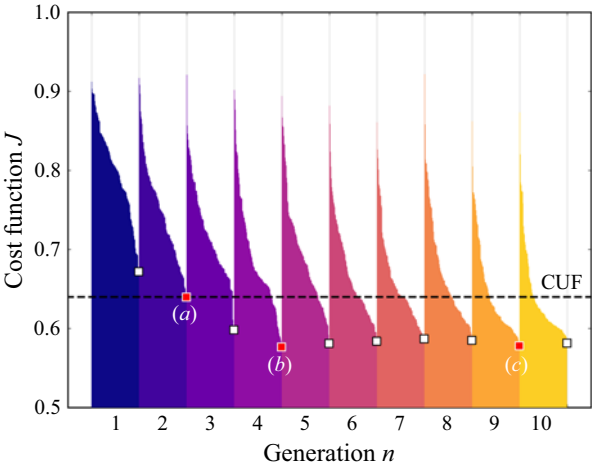


Figure 7. Learning curve (1000 individuals). The square symbol stands for the best individual in each generation. The three red squares are representative individuals, corresponding to (*a*) CUF (highlighted by a horizontal broken line), (*b*) GA solution I or GA-I and (*c*) GA solution II or GA-II, respectively.

suction associated with synthetic jets is not beneficial to the spread of the ZSM fluids in the viscous sublayer. As a matter of fact, the suction does not contribute to DR as blowing does, which will be discussed in detail in § 6.8.

5.2. *The GA-based optimization and representative control laws*

Initially 33 parameters were optimized, i.e. $\boldsymbol{V_0} = [V_{0,1}, V_{0,2}, \ldots, V_{0,11}]$, $\boldsymbol{f} = [f_1, f_2, \ldots, f_{11}]$ and $\boldsymbol{\phi} = [\varphi_1, \varphi_2, \ldots, \varphi_{11}]$. This was unfortunately unsuccessful, producing no individual that performed better than CUF. This failure is ascribed to two causes. Firstly, it is difficult to optimize such a large number of control parameters using GA. With an increase in the number of parameters, the search space grows exponentially, resulting in deteriorated search efficiency and making it a great challenge to find the global optimal or near optimal solutions. Secondly, when f_i are different from each other, the variations in φ_i is pointless, complicating the search process. As such, we reduce the control parameters to 22 and optimize only $\boldsymbol{V_0}$ and $\boldsymbol{f}$. This change led to a converged learning process, though the optimized solution was the CUF. Other than the adverse influence of excessive parameters, the root cause for the failure to identify better performed optimal solutions could be the choice of the control parameters. Streaky structures play a crucial role in the turbulence regeneration cycle. The present separation between adjacent synthetic jets is 20 l_v, and the average separation between streaky structures, with a width of $20 \sim 60l_v$ (Iuso *et al.* 2003), is $100l_v$ (Kline *et al.* 1967), implying that one to three synthetic jets manipulate one streaky structure and five take place between streaky structures. It seems plausible that a change in f_i or $V_{0,i}$ from one synthetic jet to another does not really help with the search of optimal solutions. Therefore, we decide to optimize $\boldsymbol{\varphi} = [\varphi_1, \varphi_2, \ldots, \varphi_{11}]$, with $V_{0,i}$ and f_i set at the optimal values obtained from the CUF. For periodic forcing, the actuation corresponding to $\boldsymbol{\varphi} = (\varphi_1, \varphi_2, \ldots, \varphi_{11})$ is the same as $\boldsymbol{\varphi} = (\varphi_1 - \varphi_1, \varphi_2 - \varphi_1, \ldots, \varphi_{11} - \varphi_1) = (0, \varphi_2, \ldots, \varphi_{11})$. That is, the effective parameters are reduced from 11 to 10, and φ_i ($i = 2, 3, \ldots, 11$) may vary discretely in $[0, 2\pi)$ with an increment of 0.05π.

Figure 7 presents the learning curve of the GA search for the optimum $\boldsymbol{\varphi}$, where each bar of the same colour consists of 100 costs J estimated from the 100 individuals of each generation. The square symbol highlights the lowest or best cost J_n of a generation.

https://doi.org/10.1017/jfm.2026.11625 Published online by Cambridge University Press

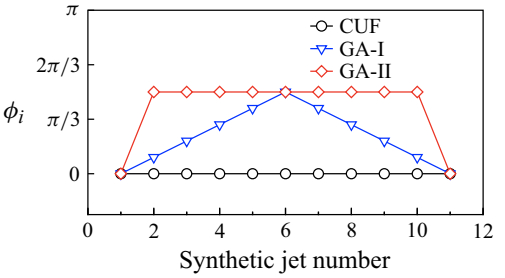


Figure 8. Initial phases ϕ_i of synthetic jets associated with three representative control laws.

The J_1 of the first generation drops substantially from 1 without control to 0.66. The CUF is identified as the best individual of the second generation with a cost function $J_2 = J_{CUF} = 0.63$, corresponding to spanwise averaged $\overline{\delta_{\tau_w}}$, $< \overline{\delta_{\tau_w}} >_s$, of –37 % measured at $x^+ = 100$, where $< >_s$ denotes the averaging value of measured local WSSs from the nine wall wire sensors. By the fourth generation, the best individual produces $J_4 = 0.57$, which seems getting converged, named GA-I. In the following generations, the lowest costs essentially do not drop further and the best individuals remain unchanged. However, the best individual of the ninth-generation changes, that is, a different control law appears, albeit with the same cost, i.e. $J_9 = 0.57$. We call it GA-II. After that, the best individuals will be either GA-I or GA-II. Note that only 40 s were used to evaluate each individual, estimating its J_i^n. Thus, there is a certain level of uncertainty in J in the learning process. This may account for a small variation from J_4 to J_{10}. At the end of the GA search, the ten best individuals of each generation were re-evaluated with a longer measurement time of 80 sec, which confirmed that GA-I and GA-II are the optimal solutions.

Three representative individuals are compared in figure 8 and the corresponding solutions are given by

$$\boldsymbol{\phi_i}^{\boldsymbol{CUF}} = (0, 0, 0, 0, 0, 0, 0, 0, 0, 0, 0), \tag{5.1a}$$

$$\boldsymbol{\phi_i}^{\boldsymbol{I}} = (0, 0.1\pi, 0.2\pi, 0.3\pi, 0.4\pi, 0.5\pi, 0.4\pi, 0.3\pi, 0.2\pi, 0.1\pi, 0), \tag{5.1b}$$

$$\boldsymbol{\phi_i}^{\boldsymbol{II}} = (0, 0.5\pi, 0.5\pi, 0.5\pi, 0.5\pi, 0.5\pi, 0.5\pi, 0.5\pi, 0.5\pi, 0.5\pi, 0). \tag{5.1c}$$

The phase distribution of the GA-I resembles an isosceles triangle. The phases of $S_1 \sim S_6$ increase from 0 to 0.5π with the same phase shift of approximately 0.1π, forming a travelling wave from S_1 to S_6. The constant phase shift between adjacent synthetic jets produces a spanwise travelling wave as Bai *et al.* (2014) did. On the other hand, the phase shift between adjacent synthetic jets is -0.1π from S_6 to S_{11}, forming a reversed travelling wave. Thus, GA-I produces two opposite spanwise travelling waves, which is a variant of the standard travelling wave, a waveform that has never been used in the control of TBLs. As for GA-II, synthetic jets from S_2 to S_{10} are synchronized, as CUF, though the phases of S_1 and S_{11} lag 0.5π behind.

The presently developed data-driven optimization technique exhibits excellent robustness; both GA-I and GA-II can be obtained irrespective of different population initializations. Nevertheless, several observations have been made when the population initialization varies. Firstly, the learning process and hence the convergence speed depend on the population initialization. The poor population initialization may lead to a rather slow convergence; a maximum of three more generations than that shown in figure 7 was observed. Secondly, CUF failed to be captured in several experiments, though individuals similar to CUF could occur. Finally, although GA-I and GA-II will always be captured,

https://doi.org/10.1017/jfm.2026.11625 Published online by Cambridge University Press

the sequential order may change, that is, GA-II can be found first, followed by GA-I. This implies different search paths associated with different population initializations.

5.3. *Local skin-friction drag variation*

As part of the control performance evaluation, we measured the longitudinal and spanwise variations of $\overline{\delta_{\tau_w}}$ under CUF, GA-I and GA-II, based on the hot-wire-measured gradient of streamwise velocity in the sublayer. In view of the symmetry about S_6 or the centreline of the three control laws (figure 8), the spanwise distribution of $\overline{\delta_{\tau_w}}$ was measured only for $x^+ \leqslant 0$ and the data for $x^+ > 0$ was mirrored from left to right in an effort to minimize the exposure of PZT membranes to high voltage and to prolong their usage.

The spanwise distributions of $\overline{\delta_{\tau_w}}$ are presented in figure 9 for a series of positions, downstream of the synthetic jets. Both GA-I and GA-II achieved a spanwise averaged DR of 52 % at $x^+ = 33$, higher than that under CUF (45 %), though their spanwise distributions of $\overline{\delta_{\tau_w}}$ are very different (figure 9*a*). The minimum DR is 75 % and 70 % under GA-I and GA-II, respectively, significantly higher than that (55 %) under CUF. The results suggest that GA-I and GA-II may have produced an even larger averaged DR over the control area than CUF. The spanwise motion in GA-I and GA-II as shown in figure 14 is the main reason for the different spanwise distributions of $\overline{\delta_{\tau_w}}$. The spanwise motion is beneficial to DR in two ways. Firstly, this motion acts to stabilize the randomly occurring streaky structures as mentioned in Cheng *et al.* (2021*b*). Secondly, the synthetic jets eject the ZSM fluids, decreasing the near-wall streamwise velocity. Both effects contribute to DR. The ZSM fluids may redistribute along the z-direction under the spanwise motion effect. The ZSM fluids move from the exits of S_1 and S_{11} towards S_6 into region R3 ($-40 < z^+ < 40$) of GA-I or R2 ($-80 < z^+ < -40$ and $40 < z^+ < 80$) of GA-II, thus achieving higher DR. As shown in figure 14, a spanwise motions of GA-I and GA-II arise in different region. The spanwise motion of GA-I is influential in R2 and carries the ZSM fluid towards R3, where the ZSM fluid largely stays due to the opposite movement on the other side of the centreline. Consequently, the DR in R3 is largest and that in R1 is smallest, where the 3-D effect is significant. As for GA-II, the spanwise motion occurs mainly near S_1 and S_{11}. The DR results from both spanwise motion effect and the presence of the ZSM fluid in R2 but is mostly due to the latter in R3, which explains why the DR is largest in R2 of the three regions. Spanwise distributions of $\overline{\delta_{\tau_w}}$ vary farther downstream, i.e. $x^+ = 100$–433 (figure 9*b*–*f*), since the spanwise motion impairs and the ZSM fluid gains momentum when interacting with surrounding flow. For example, under CUF, the two valleys in $\overline{\delta_{\tau_w}}$ obvious at $x^+ = 33$ (figure 9*a*), disappear completely at $x^+ \geqslant 166$ (figure 9*c*–*f*) probably because the asymmetric vortices generated near S_1 and S_{11} have broken up. The GA-II produces a stronger spanwise velocity at the two ends of the synthetic array and hence the two valleys in $\overline{\delta_{\tau_w}}$ remain discernible even by $x^+ = 166$. Note that the two valleys move towards the middle probably due to the spanwise motions. The DR under GA-I maintains smallest in the central region, probably because of the persisting spanwise motion, until $x^+ \approx 300$. The difference in $\overline{\delta_{\tau_w}}$ between the three control strategies starts vanishing beyond $x^+ = 433$.

The drag recovery is best reflected by the longitudinal variation of $\overline{\delta_{\tau_w}}$ measured in the plane of symmetry ($z^+ = 0$), where the flow is least affected by the 3-D effect. The variation in $\overline{\delta_{\tau_w}}$ measured in this plane differs considerably from one control strategy to another (figure 10*a*). The DR is significantly more pronounced for $x^+ < 200$ under GA-I and GA-II than under CUF, and the drag does not fully recover until $x^+ = 650$ and 550 under GA-I and GA-II, respectively, appreciably extended compared with that (500) under

https://doi.org/10.1017/jfm.2026.11625 Published online by Cambridge University Press

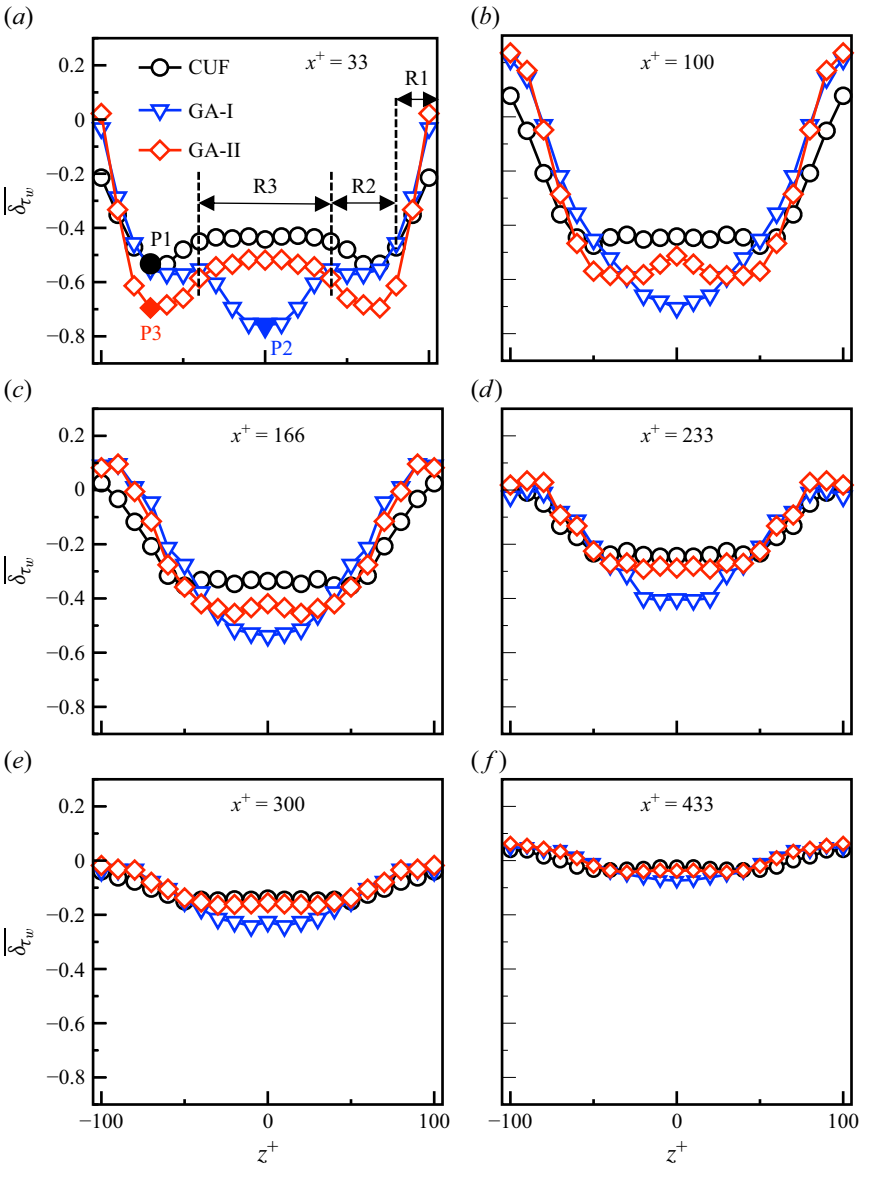


Figure 9. Spanwise distributions of the local $\overline{\delta_{\tau_w}}$ at different x^+. The solid symbols, indicated by P1, P2 and P3 in (*a*), correspond to the local maximum DR for each forcing.

CUF (figure 10*a*). Note that $\overline{\delta_{\tau_w}}$ under GA-II appears dropping from $x^+ = 33$–80, which is ascribed to the shift in its valleys towards the centreline (figure 9). However, the DR performance should be evaluated from the spanwise-averaged $\overline{\delta_{\tau_w}}$ at each longitudinal location, *viz.*

$$\langle \overline{\delta_{\tau_w}} \rangle_z = \frac{\int_{z_1^+}^{z_2^+} \overline{\delta_{\tau_w}} \, \mathrm{d}z}{z_2^+ - z_1^+}, \tag{5.2}$$

https://doi.org/10.1017/jfm.2026.11625 Published online by Cambridge University Press

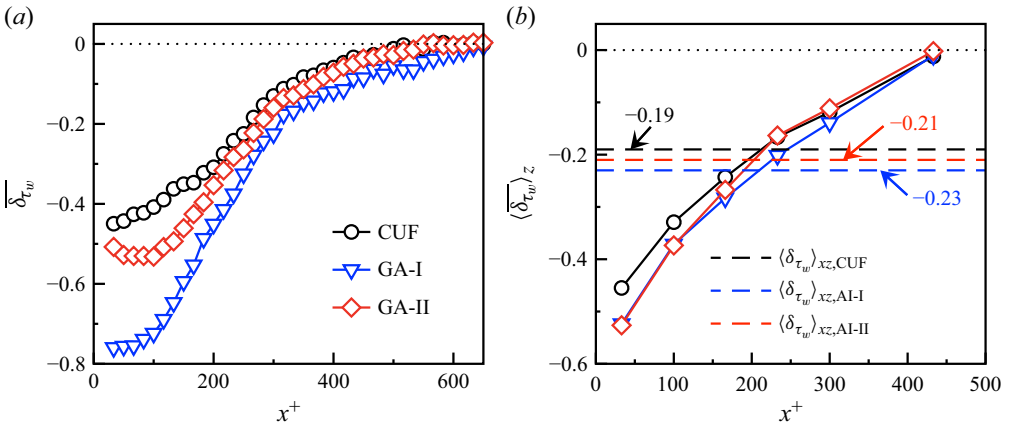


Figure 10. Downstream variations of (*a*) the local $\overline{\delta_{\tau_w}}$ measured at $z^+ = 0$, and (*b*) the spanwise-averaged DR ($U^+_{jet,max} = 4, f^+ = 0.71$).

where $\langle\rangle_z$ denotes spanwise-averaging, z_1^+ and z_2^+ are –100 and 100, corresponding to the two ends of the synthetic jet array. The $\langle\overline{\delta_{\tau_w}}\rangle_z$ is essentially the same under GA-I and GA-II, which is smaller than under CUF at $x^+ \leqslant 200$ (figure 10*b*). The result is internally consistent with the same cost function under GA-I and GA-II, which is considerably smaller than under CUF (figure 7). Beyond $x^+ > 200$, $\langle\overline{\delta_{\tau_w}}\rangle_z$ of GA-II collapses with that of CUF, while $\langle\overline{\delta_{\tau_w}}\rangle_z$ of GA-I continues to outperform that of CUF until $x^+ = 433$, where the drag is close to full recovery, irrespective of the control strategy.

We may estimate the 'total' DR downstream of the actuator by the longitudinal integration of $\langle\overline{\delta_{\tau_w}}\rangle_z$ from $x^+ = 33$ to $x^+ = 433$, *viz.*

$$\langle\overline{\delta_{\tau_w}}\rangle_{xz} = \frac{\displaystyle\int_{x_1^+}^{x_2^+} \langle\overline{\delta_{\tau_w}}\rangle_z \,\mathrm{d}x}{x_2^+ - x_1^+}. \tag{5.3}$$

The values of $\langle\overline{\delta_{\tau_w}}\rangle_{xz}$ under CUF, GA-I and GA-II are –19 %, –23 % and –21 %, respectively (figure 10*b*). Here GA-I produces the largest 'total' DR with the slowest drag recovery rate, which is attributed to the presence of a wider range ($-90 < z^+ < -20$ or $20 < z^+ < 90$) of spanwise velocity as evidenced in figure 14.

5.4. *Control landscape: cartographing all actuation laws*

The proximity map provides a visual perspective of the evolution of the individuals. Figure 11 presents the proximity map of four representative generations ($n = 1, 2, 4, 9$) and all individuals in the phase plane (γ_1, γ_2), which are calculated as discussed in § 4.4. The distance between two points quantifies the extent to which two control laws resemble each other. For $n = 1$ (figure 11*a*), the individuals appear rather randomly distributed in the sample space. The individuals with low cost functions arise mostly in the left-hand region. At $n = 2$ (figure 11*b*), the search for better solutions begins to focus on the left-hand side. In region 1, the optimal solution of this generation, CUF, occurs at $(\gamma_1, \gamma_2) = (-0.99, 0.28)$, where γ_1 is the smallest of all points. Additionally, individuals with small cost functions are found in regions 2 and 3. At $n = 4$ (figure 11*c*), GA-I at $(\gamma_1, \gamma_2) = (-0.61, 0.22)$, with a lower cost function or $\overline{\delta_{\tau_w}}$ is identified in region 2. Beyond $n = 4$, the best

https://doi.org/10.1017/jfm.2026.11625 Published online by Cambridge University Press

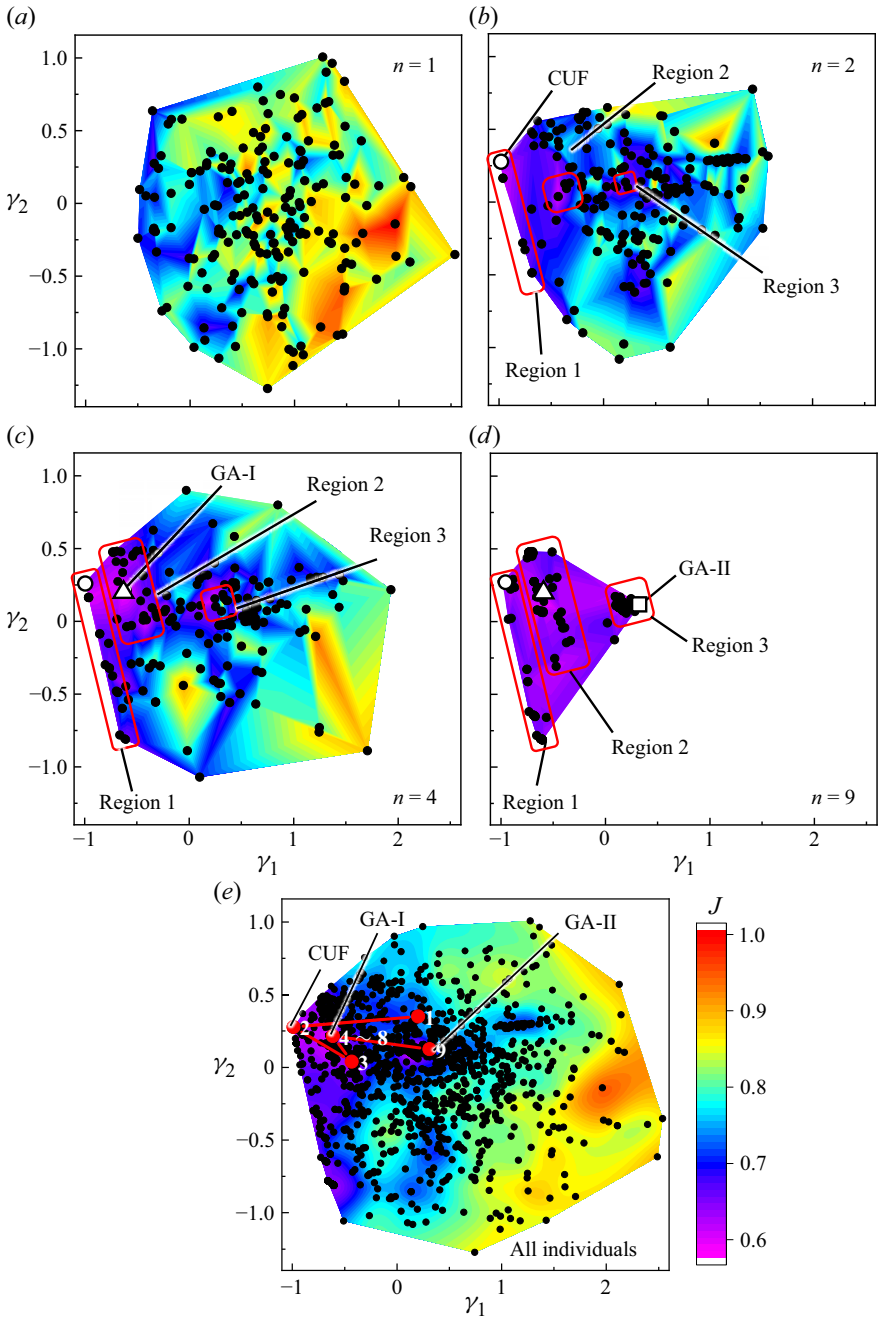


Figure 11. Control landscape associated with generations 1, 2, 4 and 9 (400 individuals) and all individuals. Each black solid point corresponds to an individual in one generation. The open symbols highlight the occurrence of CUF, GA-I or GA-II. Each red-coloured rectangle encloses similar individuals. The red lines in figure 11(*e*) connect the optimal solutions (red solid circles) in each generation.

https://doi.org/10.1017/jfm.2026.11625 Published online by Cambridge University Press

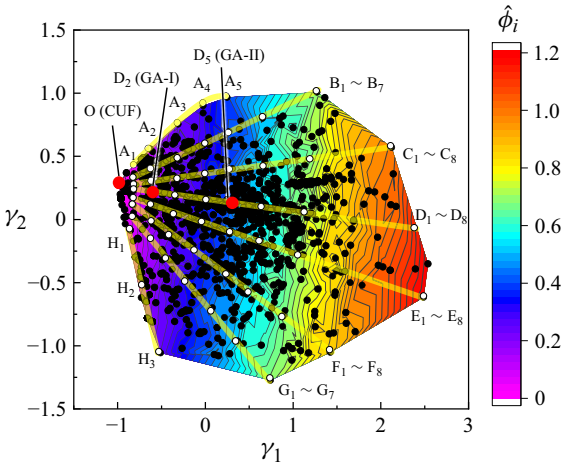


Figure 12. Control landscape associated with all generations, including 1000 individuals. Each symbol represents an individual. The colour scheme corresponds to the averaged ϕ_i of each individual. The individuals along the yellow lines will be closely examined in figure 13.

individual J_n of a generation appears converged. Interestingly, at $n = 9$, an individual GA-II, is discovered at $(\gamma_1, \gamma_2) = (0.32, 0.12)$ in region 3. Figure 11(*e*) provides a full picture for the control landscape, where the red line denotes the path of the optimal solutions in each generation. The optimal solution from one generation to another varies rather greatly and moves backwards and forwards in terms of γ_1 and γ_2, demonstrating that the optimization process is not trapped locally and is capable of exploring the unknown regions that potentially contains the global optimal solution. For instance, from generation 4–8, the optimal solutions are already converged, all identified as GA-I. However, in generation 9 the search jumps out of region 2, where this 'globally optimal solution' occurs, and discovers another globally optimal solution, GA-II, in region 3.

Derived from a mathematical optimization process based on the Euclidean distance between individuals, γ_1 and γ_2 do not have *a priori* meaning. However, a careful analysis of control laws suggests that γ_1 is correlated with the averaged ϕ_i, while γ_2 is linked to the degree of asymmetry of the phase distribution. The dependence of spatially averaged ϕ_i, $\widehat{\phi_i}$, associated with each individual on γ_1 and γ_2 is presented in figure 12, where all 1000 individuals are included. The individual for CUF, with the smallest $\widehat{\phi_i}$ $(= 0)$, occurs at the smallest γ_1 of all individuals. The variation in $\widehat{\phi_i}$, as reflected by the changing colour, is closely correlated with γ_1. To understand γ_2, we show in figure 13 the phases of the synthetic jets for those points marked in figure 12. The individuals with comparable $\widehat{\phi_i}$ are allocated with the same subscript number. Interestingly, the phase distribution of individuals from group A to H seems to shift gradually from the left-skewed appearance to the right-skewed, and individuals D_1 to D_8 exhibit approximately symmetrical phase distributions about S_6. The sinusoidal travelling wave is a classical and popular strategy used in the TBL control (e.g. Du & Karniadakis 2000; Bai *et al.* 2014). Evidently, individual C_8 that occurs in the second generation is similar to a sinusoidal travelling wave. Yet, its control effectiveness is poorer than CUF. This is not surprising. As Bai *et al.* (2014) noted, the longer the wavelength, the better the control performance, and CUF can be regarded as a travelling wave with an infinite wavelength.

https://doi.org/10.1017/jfm.2026.11625 Published online by Cambridge University Press

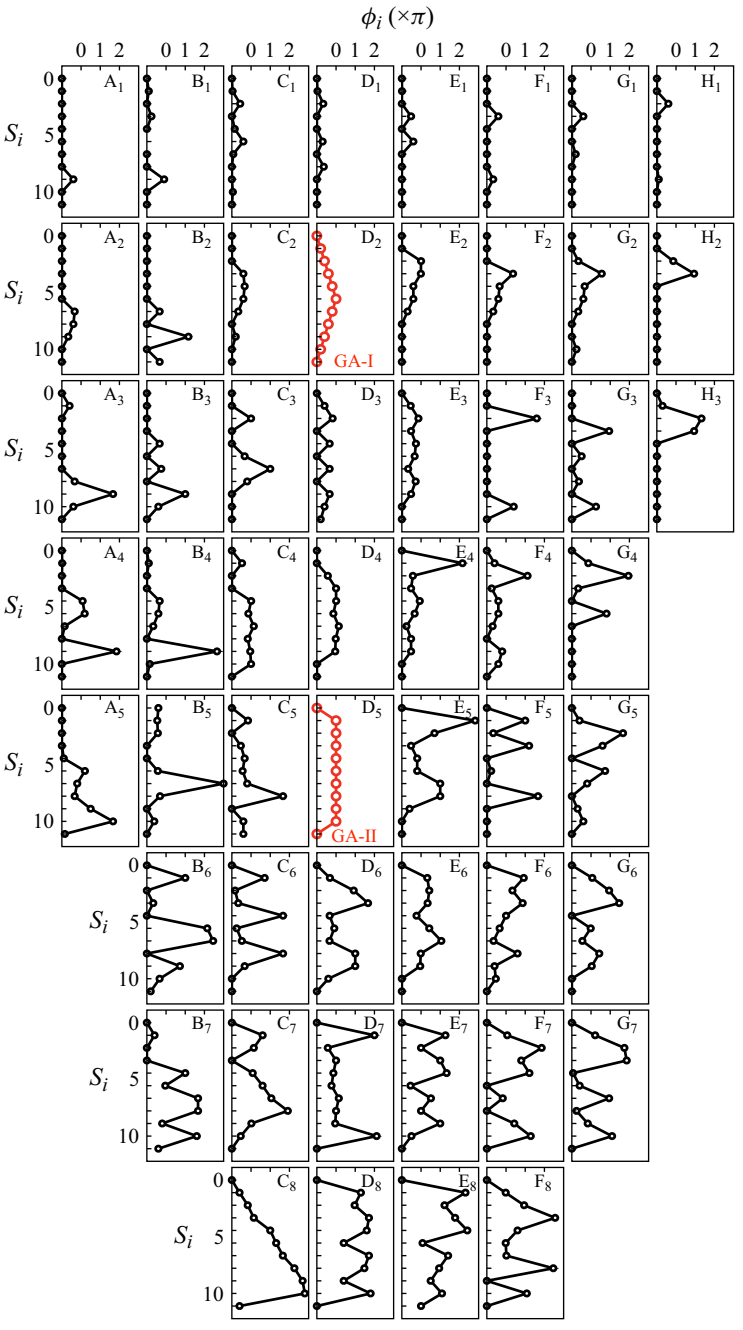


Figure 13. Phases associated with individuals along the yellow lines in figure 12. The symbols are as in figure 12.

6. Discussion: modified flow structure and DR mechanisms

6.1. *Synthetic-jet-induced flow*

It is important to document the synthetic-jet-induced flow, which is crucial for understanding the flow physics behind effective control. Using the same actuator, Yu,

https://doi.org/10.1017/jfm.2026.11625 Published online by Cambridge University Press

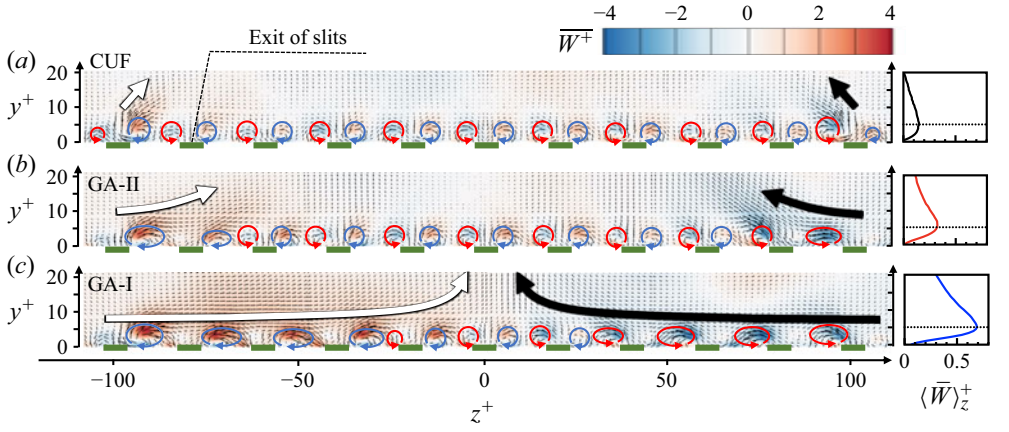


Figure 14. The PIV-measured spanwise velocity $\overline{W^+}$ and velocity vectors ($\overline{V^+}$, $\overline{W^+}$), time-averaged out of 2700 images, in the y–z plane of $x = -12$ mm. The green rectangles at the bottom of each panel mark the position of the slits. The red and blue circular arrows show the senses of the streamwise vortices resulting from the synthetic jets, while the black and white arrows highlight spanwise motions. The different sizes of the circular arrows denote a variation in the size of vortical structures. The wall-normal distributions of spanwise-averaged $\overline{W^+}$, i.e. $\langle\overline{W}\rangle_z^+$, for $-120 < z^+ < 0$ are given on the right side of the velocity vector plots.

Mi & Zhou (2025) investigated the evolution of a single synthetic jet with the same actuation frequency and amplitude in one cycle. It is found that there are three stages in a synthetic jet cycle, i.e. blowing, suction and producing counter-rotating streamwise vortices (CRSVs). Due to the presence of suction, the CRSVs do not move away from the wall with the blowing process. The generation of small-scale CRSVs usually occurs in unsteady blowing or synthetic jets through the longitudinal slit (Rathnasingham & Breuer 2003; Cheng *et al.* 2021*a*). In figure 14, the PIV-measured flow structures generated by synthetic jets array under different actuation strategies are compared in the absence of incident flow. Under CUF, one array of CRSVs is generated at $-90 < z^+ < 90$ with a height of approximately five wall units, comparable to the viscous sublayer thickness. Interacting with CRSVs only on one side, the pair of CRSVs at each end, $z^+ = -100$ or 100, of the array appears skewed, inducing an obvious spanwise motion at $z^+ \approx \pm$ 95, as indicated by an arrow. For two GA solutions, spanwise motions are enhanced because of the presence of a phase shift between adjacent synthetic jets. The effect of phase difference on instantaneous jet distribution and interactions has been rather thoroughly discussed in Yu *et al.* (2025). Briefly, it is found that dual synthetic jets at high Strouhal numbers may induce a spanwise motion when there is a phase difference between them, and this motion is strongest at a phase difference of 0.5π. This motion will be significantly enhanced when the number of synthetic jets increases to three given the same phase shift. The mechanism of this spanwise motion is also discussed in detail. The wall-normal distribution of the spanwise-averaged $\overline{W^+}$, i.e. $\langle\overline{W}\rangle_z^+$ (figure 14), over $-120 < z^+ < 0$ indicates the occurrence of the maximum $\langle\overline{W}\rangle_z^+$ at $y^+ = 5$. The ensuing $\overline{|W_{max}|}^+$ measured at $(y^+, z^+) \approx (5, \pm 90)$ is found to be 3.9 for GA-I, which agrees very well with previous findings. The spanwise velocity makes a positive contribution to DR. Schoppa & Hussain (1998) observed that spanwise blowing in the viscous sublayer of a turbulent channel flow resulted in a 20 % DR, which suppressed the underlying streak instability mechanism and hence near-wall longitudinal vortices. Yao *et al.* (2017, 2018) and Cheng *et al.* (2021*b*) investigated the relation between DR and maximum

https://doi.org/10.1017/jfm.2026.11625 Published online by Cambridge University Press

spanwise velocity $\overline{|W_{max}|}^{+}$ and found that the optimal control performance was achieved when $\overline{|W_{max}|}^{+}$ was approximately four times the friction velocity. Note that the opposed travelling waves of GA-I induce opposite spanwise motions. On the other hand, under GA-II which can be considered to be a variant of CUF, the spanwise motion enhances two larger vortices at $z^{+} \approx \pm 90$, as under CUF, and $\overline{|W_{max}|}^{+}$ increases from 2.0 at $(y^{+}, z^{+}) \approx (5, \pm 95)$ to 3.5 at $(y^{+}, z^{+}) \approx (5, \pm 90)$.

6.2. *Interactions between synthetic-jet-induced flow and TBL*

To gain insight into the interactions between the synthetic-jet-induced flow and incident TBL, we examine the spectral coherence $Coh_{u_iu_{i+1}}$ $(i = 1 \sim 8)$ between fluctuating streamwise velocities u_i and u_{i+1} from adjacent wall wires, W_i and W_{i+1}, with and without control (figure 15). The magnitude of $Coh_{u_iu_{i+1}}$ reflects the degree of correlation between u_i and u_{i+1}, ranging from 0 to 1, where 0 means no correlation and 1 means a perfect correlation. The high correlation between two hot-wire signals indicates that both hot-wires have detected the same flow structures. In the near-wall region of the TBL (the linear and buffer layers), QSVs and streaky structures are predominant (Robinson 1991). The average width of these streaky structures is of the order of $60l_v$ (Iuso *et al.* 2003), and the diameters of the QSVs is $30l_v$ (Robinson 1990). The present distance between adjacent wall wires is $20l_v$, implying that the large-scale coherent structures, i.e. the streaky structures or QSVs larger than this scale, will be responsible for this high $Coh_{u_iu_{i+1}}$. Note that the coherence structure is a large-scale and low-frequency motion. For example, the low-speed streaks associated with QSVs are responsible for the bursting events, characterized by a frequency f^{+} of approximately 0.004 (Blackwelder & Haritonidis 1983).

In the natural TBL (figure 15*a*), $Coh_{u_iu_{i+1}}$ $(i = 1, 2, \ldots, 8)$ appear similar to each other and the large value at $f^{+} < 0.01$ is apparently linked to the presence of large-scale structures. Under control, the $Coh_{u_iu_{i+1}}$ varies significantly. Since CUF, GA-I and GA-II, are all symmetric about S_6, $Coh_{u_iu_{i+1}}$ should be symmetric about wall wire W_5 as well. A few observations can be made under control. Firstly, under CUF, $Coh_{u_1u_2}$ and $Coh_{u_8u_9}$ are smallest of all, which is attributed to the 3-D effect. Here $Coh_{u_4u_5}$ and $Coh_{u_5u_6}$ about W_5 are appreciably smaller than $Coh_{u_2u_3}$, $Coh_{u_3u_4}$, $Coh_{u_6u_7}$ and $Coh_{u_7u_8}$ for low frequencies, $f^{+} < 0.1$. Secondly, under GA-I and GA-II, the differentiation between the three groups of $Coh_{u_iu_j}$ is qualitatively the same as under CUF. However, the frequency band where $Coh_{u_2u_3}$, $Coh_{u_3u_4}$, $Coh_{u_6u_7}$ and $Coh_{u_7u_8}$ are large, say beyond 0.4, broadens appreciably because the spanwise motion induced by GA-I or GA-II acts to stabilize the randomly occurring streaky structures and this motion is strongest in these positions. Again, $Coh_{u_1u_2}$ and $Coh_{u_8u_9}$ are adversely affected by the 3-D effect, and $Coh_{u_4u_5}$ and $Coh_{u_5u_6}$ suffer from the clash between two opposite spanwise motions (figure 14), which is not beneficial to stabilizing streaky structures. Thirdly, $Coh_{u_4u_5}$ and $Coh_{u_5u_6}$ are lower under GA-I than under GA-II, suggesting that the former produces a stronger spanwise motion than the latter in these positions, probably because the two opposite spanwise motions clash against each other more violently under GA-II. Finally, the above observations indicate that the spanwise motion generated by control persists downstream of the actuators since the measurement is made at $x^{+} = 100$.

6.3. *Mean and fluctuating streamwise velocities*

Figure 16(*a*,*b*) presents the mean streamwise velocity distributions along the y-direction normalized by actual inner and outer scales, separately, for CUF, GA-I and GA-II.

https://doi.org/10.1017/jfm.2026.11625 Published online by Cambridge University Press

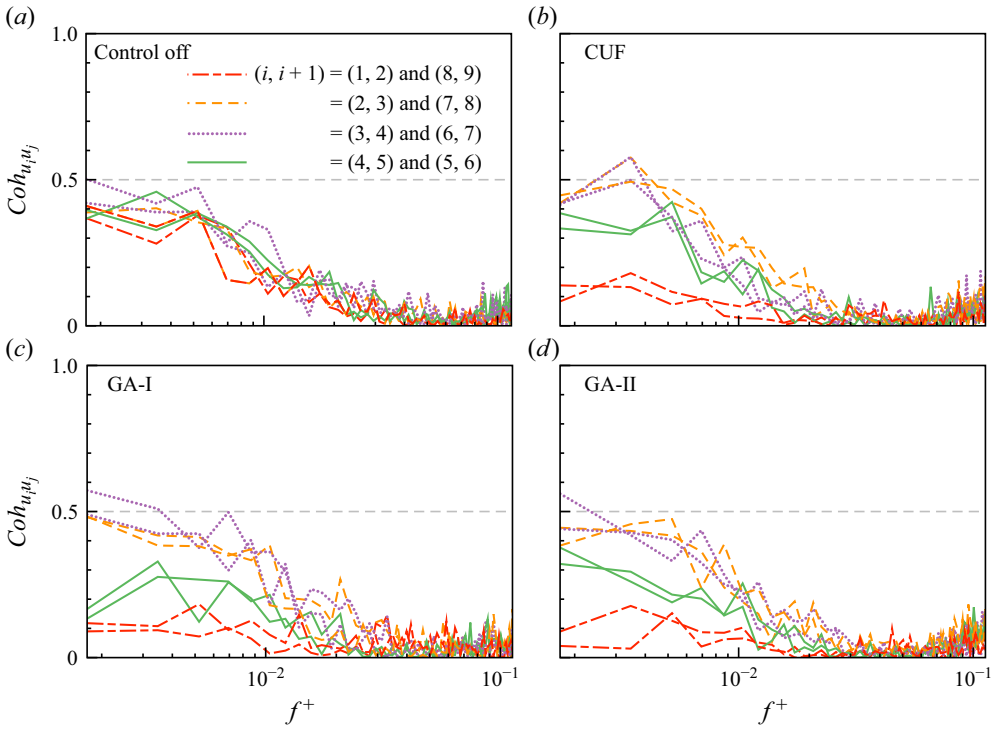


Figure 15. Spectral coherence Coh_{uiuj} between fluctuating velocities u_i and u_j measured from adjacent wall-wires W_i and W_j ($x^+ = 100$). The spanwise separation between the two wall-wires is 20 wall units, and the wall wires are 3.3 wall units away from the wall.

The measurements were taken at P1, P2 and P3 (figure 9*a*), i.e. $(x^+, z^+) = (33, -70)$, (33, 0) and (33, –70), where the maximum DR occurs for the three control strategies. In the absence of control, the $\overline{U^+}$ profile (figure 16*a*) satisfies the law of wall (red line), i.e. $\overline{U^+} = y^+$ in the viscous sublayer ($y^+ < 5$), and $\overline{U^+} = 2.44\ \ln y^+ + 5.1$ in the logarithmic region ($30 < y^+ < 170$), suggesting that the uncontrolled TBL is fully developed. When manipulated, the $\overline{U^+}$ profiles normalized by the actual inner scale adhere to $\overline{U^+} = y^+$ in the viscous sublayer for all three control strategies (figure 16*a*). The logarithmic regions of the three controlled TBLs (figure 16*a*) are shifted upwards and slightly inclined, suggesting a smaller value of the von Kármán constant compared with the natural TBL. The upward shift in the logarithmic region is typical for most of the skin-friction-reduced flow (e.g. Choi 1989). While normalized by the outer scale (figure 16*b*), i.e. U_∞ and δ_{99}, the near-wall $\overline{U^*}$ reduces most under GA-I, followed by GA-II and then CUF in the liner region, which is internally consistent with the observation from figure 9*a*. The $\overline{U^*}$ profiles remain unchanged with control for $y^* > 0.07$ or $y^+ > 40$ (figure 16*b*), that is, the logarithmic and outer regions are little affected, as noted by Cheng *et al.* (2021*a*).

The root mean square (r.m.s.) value ${u_{rms}}^+$ of the fluctuating streamwise velocity u is much larger than its counterpart of the natural TBL at $y^+ < 230$ (figure 16*c*) due to a significant change in the local inner scales under control. In contrast, ${u_{rms}}^*$ decreases significantly in the near-wall region (figure 16*d*), indicating reduced turbulence intensities, in agreement with the substantial DR. Furthermore, the ${u_{rms}}^*$ values in the viscous sublayer drop most for GA-I, followed by GA-II and then CUF, in consistency with their DR levels. The QSVs and streaky structures are the sources of streamwise turbulent

https://doi.org/10.1017/jfm.2026.11625 Published online by Cambridge University Press

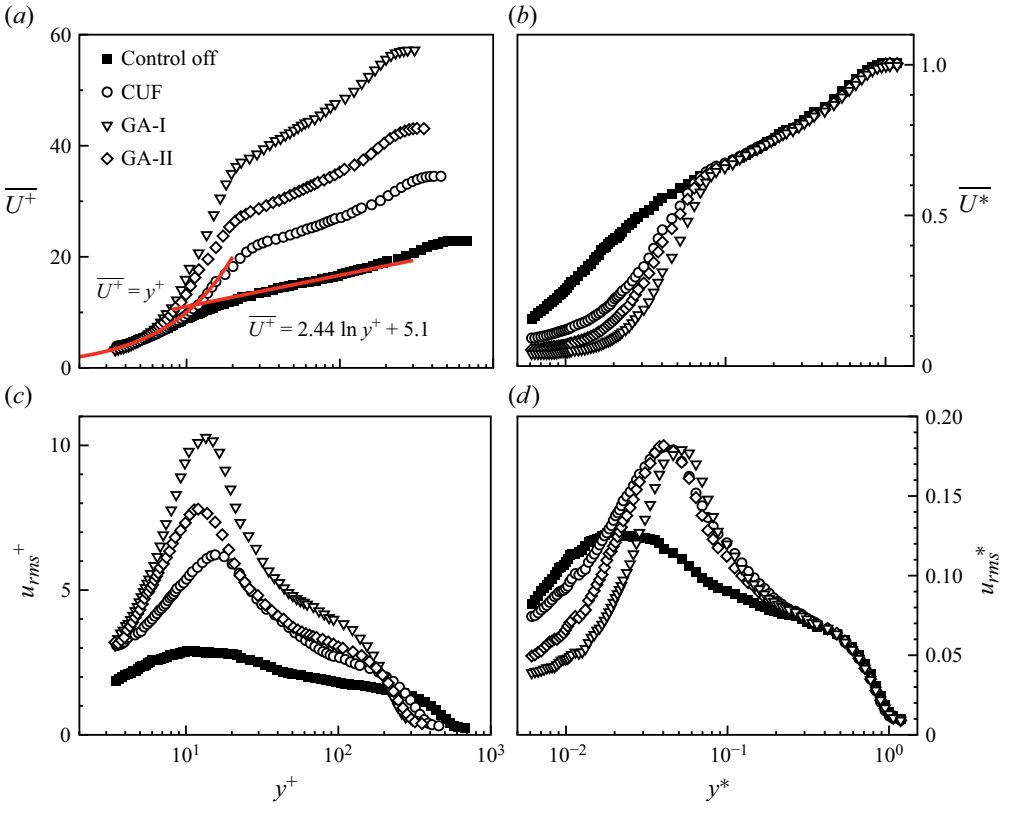


Figure 16. Wall-normal distributions of the mean streamwise velocity and corresponding r.m.s. values measured at the positions corresponding to P1, P2 and P3 in figure 9(*a*), respectively, given in (*a*) $\overline{U^+}$, (*b*) $\overline{U^*}$, (*c*) $u_{rms}{}^+$, (*d*) $u_{rms}{}^*$. The uncontrolled data are also given as a reference. The red curves show the law of the wall of the natural TBL.

intensity near the wall, as proposed in the turbulence regeneration cycle theory (Robinson 1991; Schoppa & Hussain 2002). Thus, the diminished $u_{rms}{}^*$ values under control imply the stabilized coherent structures and inhibited turbulence regeneration cycle. The lower $u_{rms}{}^*$ of GA-I and GA-II in the near-wall region suggest more stabilized streaky structures or QSVs, which is connected to the spanwise motion under these two control modes, as discussed in § 6.1. With increasing y^+, the $u_{rms}{}^*$ value gradually exceeds its counterpart of the natural TBL, peaking at $y^* = 0.04$ ($y^+ = 23$), 0.052 (29) and 0.046 (26) under in CUF, GA-I and GA-II, respectively, well above that ($y^* = 0.02$ or $y^+ = 11$) in the natural TBL. The shift in the $u_{rms}{}^*$ peak under control, as shown in figure 18(*d*), is common in the TBL control involving blowing or suction. Park & Choi (1999) found that the uniform blowing injected ZSM fluid into the TBL and lifted the QSVs, causing the outward shift in the $u_{rms}{}^*$ peak, while the suction did the opposite. The lifted QSVs grew downstream in strength, resulting in an increase in turbulence intensity so that the outward-shifted peak was accompanied by an increase in $u_{rms}{}^*$ (Park & Choi 1999). Cheng *et al.* (2021*a*) made a similar observation and ascribed the lifted QSVs to the injection of ZSM fluids. The present synthetic jets include both blowing or suction and their durations are the same. However, since the blowing intensity is greater than the suction intensity (figure 4), the overall effect of blowing on the QSVs overwhelms the adsorption effect of suction, thus causing the QSVs to be lifted. Using an array of distributed round synthetic jets to

https://doi.org/10.1017/jfm.2026.11625 Published online by Cambridge University Press

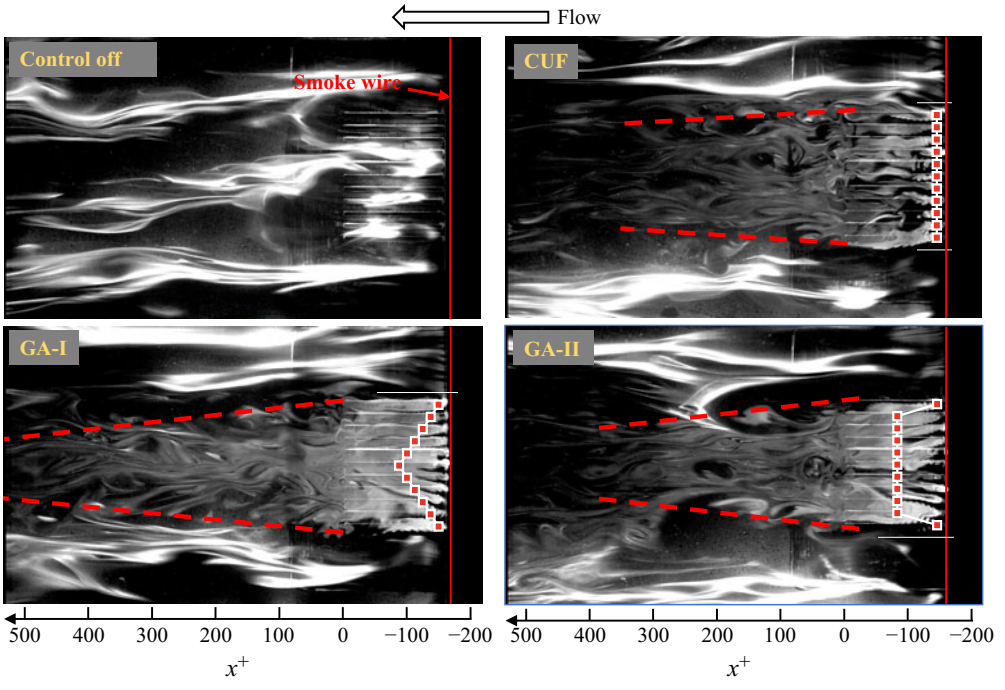


Figure 17. Typical instantaneous flow structure captured from smoke-wire flow visualization ($U_\infty = 1.8\,\mathrm{ms}^{-1}$) in the x–z planes. The smoke-wire and the laser sheet are placed at $y^+ = 5$ and 7, respectively, upstream of the synthetic jets. The broken red lines enclose roughly the low-speed streaks generated because of force. The red squares indicate the initial phases of the synthetic jets.

manipulate a TBL, Lu *et al.* (2020) also observed the outward shift in u_{rms} and ascribed the observation to the lifted coherence structures. Under GA-I and GA-II, the spanwise motion carries more ZSM fluid into the measurement position, thus QSVs are pushed even farther away from the wall, corresponding to a further shift in the $u_{rms}{}^*$ peak, compared with CUF.

6.4. *Visualized flow structure*

The near-wall flow structure may be captured through smoke-wire flow visualization in order to gain insight into the underlying flow physics behind DR. Figure 17 presents the typical images of the near-wall flow from flow visualization in the x–z plane with and without control. Since the flow is illuminated by the laser sheet in the (x, z) plane of $y^+ = 7$, smoke filaments originating from the smoke wire, placed at $y^+ = 5$, rise and track the QSVs, forming the low-speed streaks. On the other hand, the high-speed sweep events are not associated with seeding particles to be illuminated by the laser sheet, resulting in high-speed streaks. In the absence of control, the low-speed streaks occur randomly and appear quite unstable. Under CUF, the large-scale high- and low-speed streaks disappear, replaced by smaller-scale longitudinally orientated structures, which are rather stable, as enclosed by the two broken lines. Deploying blowing minijets, Cheng *et al.* (2021*a*) also observed stabilized small-scale longitudinal structures, which even exhibited a signature of local relaminarization. There is presently no obvious sign for local relaminarization. Additionally, the proportion of illuminated white-coloured small-scale streaks increased significantly, indicating that more fluids are lifted and captured

https://doi.org/10.1017/jfm.2026.11625 Published online by Cambridge University Press

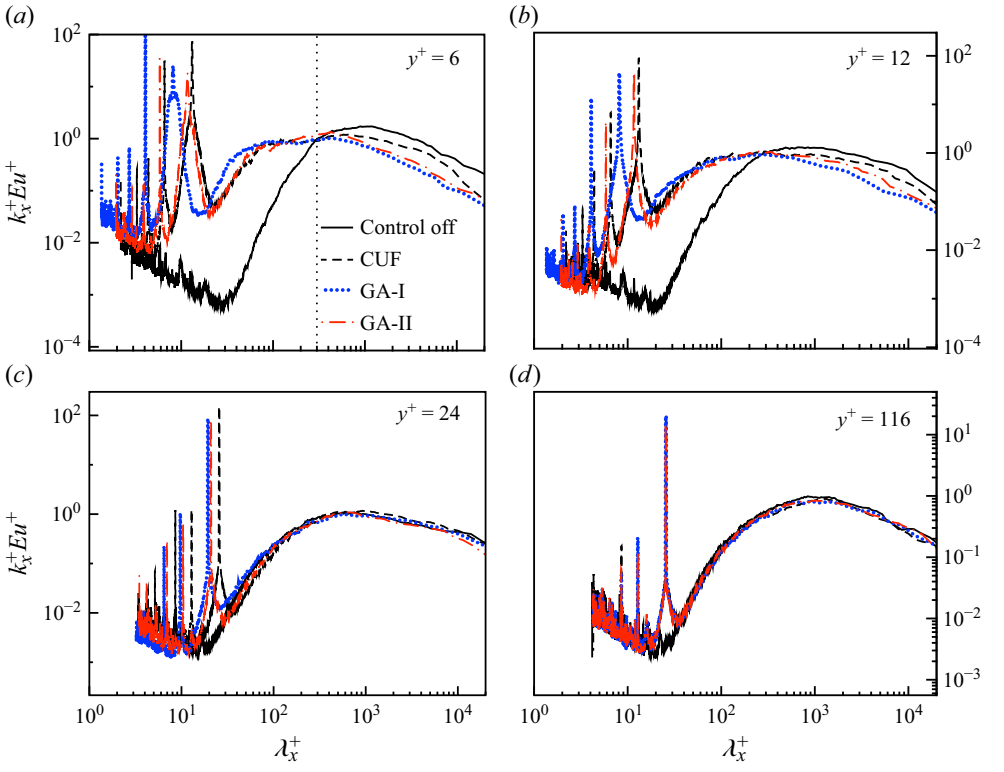


Figure 18. Premultiplied energy spectra of the fluctuating velocity u, measured at $x^+ = 33$ using a hot-wire, placed at P1, P2 and P3, as indicated in figure 9(*a*).

by the laser sheet. This observation provides additional evidence for the lifted near-wall coherent structures discussed in § 6.3. Note that the small-scale streaky structures display a slight tendency to move towards the centre, which is attributed to the 3-D effect, internally consistent with the downstream development of spanwise distribution of $\overline{\delta_{\tau_w}}$ (figure 9). Under GA-I, the flow region over the control area appears more stabilized and white-colour-dominated, apparently due to considerably stronger spanwise motions (figure 14). The white-coloured small-scale streaks downstream of the synthetic jet array are appreciably pushed towards the central region and persist longer downstream than under CUF. The results are in consistence with the more pronounced DR and longer drag recovery region than under CUF (figures 9 and 10). A similar observation can be made under GA-II, though the low-speed white-colour-dominated region, comparable to that under CUF, does not persist so long as that under GA-I as the spanwise-motion is initiated only at the two ends of the synthetic jet array.

The theoretical basis for TBL DR via spanwise motion stems from the self-sustaining cycle of near-wall turbulence and the streak transient growth (STG) theory (Schoppa & Hussain 2002). It is now well established that a spanwise motion may act to homogenize the spanwise distribution of the local streamwise velocity, i.e. reducing $\partial U/\partial z$, thereby stabilizing streaky structures and suppressing the generation of wall-normal vorticity ω_y (Yao, Chen & Hussain 2018; Thomas *et al.* 2019; Duong *et al.* 2021; Cheng *et al.* 2021*b*). This weakens the disturbance energy essential to STG, thus inhibiting the self-sustaining cycle of near-wall turbulence and leading to DR. Notably, (Jeong *et al.* 1997; Schoppa & Hussain 2002) reported that the maximum spanwise velocity was typically located at

https://doi.org/10.1017/jfm.2026.11625 Published online by Cambridge University Press

$y^+ \sim 20$–30, where streak structures are lifted away from the wall. In contrast, the GA-I strategy discovered presently generates the maximum spanwise velocity in the viscous sublayer ($y^+ \approx 5$). As shown in figure 17, under GA-I, the randomly occurring unstable streaky structures at $y^+ = 7$ become smaller-scale streaks that are more stable and spanwise uniform. This change also significantly reduces $\partial U/\partial z$. Since the streaky structures in the viscous sublayer serve as the 'seeds' for the formation and development of streak structures in the overlying buffer layer (Schoppa & Hussain 2002), modifying their morphology and stability can effectively suppress STG and disrupt the turbulence regeneration cycle.

6.5. *Redistributed energy of turbulent structures*

It can be insightful to find out how the fluctuating energy of u may redistribute in the wavenumber space under control. In figure 18 the premultiplied energy spectra $k_x E_u$ are plotted against streamwise wavelength, $\lambda_x \equiv 2\pi/k_x$, at $x^+ = 33$ for $y^+ = 6$, 12, 24 and 116, with and without control, where the wavenumber $k_x = 2\pi f/U_c$ and U_c is the convention velocity of the turbulent fluctuations. Noted that U_c depends on the distance from the wall. In the outer region, U_c is very close to the local mean velocity but exhibits a departure in the near-wall region (Quadrio & Luchini 2003). Then, we determine U_c in the near wall region following the suggestion of Quadrio & Luchini (2003). Here E_u is calculated using a fast Fourier transform with a window size of 2048 and is normalized so that its integration over the entire frequency range is unity. In the absence of control, the energy is primarily concentrated in the turbulent fluctuations with ${\lambda_x}^+ \approx 10^2 \sim 10^4$. The peak in ${k_x}^+ {E_u}^+$ occurs at ${\lambda_x}^+ \approx 1000$, corresponding to the length scale of the streaky structures (Kline *et al.* 1967). Under CUF, the energy shifts significantly to lower wavelengths or higher wavenumbers, i.e. $f^+ > 0.1$, for $y^+ \leqslant 12$, indicating an energy transfer from large- to small-scale turbulent structures (figure 18*a,b*) and reconfirming the observation from flow visualization in figure 17, where the randomly occurring large-scale near-wall streaky structures in the natural TBL are replaced by small-scale structures. A similar observation was also made by Cheng *et al.* (2021*a*) who achieved substantial DR using unsteady blowing. The spikes in low wavelength region result from the applied high frequency synthetic jets and its harmonics. Under GA-I and GA-II, the energies associated with large-scale turbulent structures are even smaller at $y^+ \leq 12$ as the strong spanwise motion stabilizes further the near-wall streaky structures. At $y^+ = 24$, the energy distribution of the three cases appears returning to its natural state; although the spikes caused by high-frequency actuation remains, the actuation does not seem to be sufficiently strong to alter the energy distribution (figure 18*c*). At $y^+ = 116$ (figure 18*d*), the spectra display a reasonable collapse despite the presence of the spike, suggesting a negligibly small effect of control on the turbulent structures. A possible scenario causing this redistribution of the turbulent flow structure scales at $y^+ \leq 12$ is proposed here. The suction inhales the near-wall fluids, including streaky structures and QSVs, into the chamber, resulting in a decrease in the energies of both large- and small-scale turbulent structures. Then, the injected fluid and CRSVs induced in the blowing phase interact with the near-wall flow structures, accounting for an increase in the energies of the small-scale structures.

6.6. *Weakened bursting events*

Bursting events play a crucial role in the TBL as a source of TKE and are closely associated with near-wall flow structures. The events may be detected from the hot-wire signals using the variable-interval time-average (VITA) technique (Blackwelder & Kaplan 1976). Two important parameters, namely the threshold k and the averaging duration T^+, must

https://doi.org/10.1017/jfm.2026.11625 Published online by Cambridge University Press

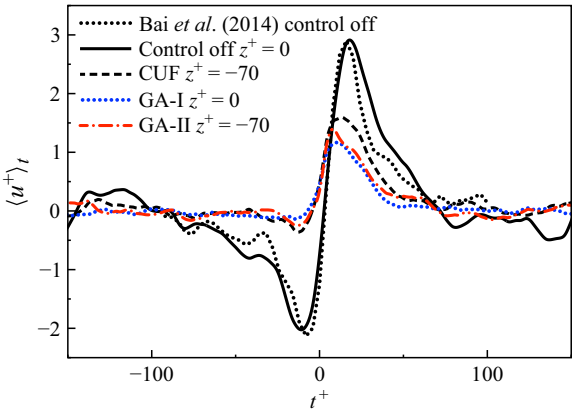


Figure 19. Ensemble-averaged streamwise fluctuating velocity $\langle u^+ \rangle_t$ based on VITA detections from the hot-wire signal measured at $(x^+, y^+) = (33, 6.5)$. The VITA parameters are $k = 0.8$, $T^+ = 38$.

be chosen carefully to ensure reasonably accurate detection. The threshold k is used to determine whether a fluctuation could be large enough to be identified as a burst event. In general, the detected burst frequency $f_b{}^+$ will gradually decrease with an increase in k. Blackwelder & Kaplan (1976) chose $k = 1$ for natural TBL. Under control, the burst intensity is weakened. As a result, the k value should be reduced. We set $k = 0.8$ following the choice of Bai *et al.* (2014). The VITA process is essentially a low-pass filter with $1/T^+$ or f^+ representing the cutoff frequency and gives a localized temporal measure of the quantity. Therefore, the choice of T^+ needs to be optimized based on the time scale of the flow. Blackwelder & Kaplan (1976) chose $T^+ = 10$ for the natural TBL. In the present case, more small-scale structures ($\lambda_x{}^+ < 300$ or $f^+ = U_c/\lambda_x{}^+ > 0.033$) are excited, as evident in figure 18, by the synthetic jets. Thus, in order to detect correctly the burst events, $T^+ = 1/f^+$ should be higher than 30 to filter out the excited small-scale structures. Bai *et al.* (2014) encountered a similar problem in their TBL control experiments and chose $T^+ = 38$ after trial and error. The present Re_θ is close to that in Bai *et al.* (2014). So is the excitation frequency. Therefore, we also chose $T^+ = 38$.

Figure 19 presents the ensemble-averaged u, i.e. $\langle u^+ \rangle_t$, at $(x^+, y^+, z^+) = (33, 6.5, 0)$ based on the VITA detections. In the absence of control, $\langle u^+ \rangle_t$ agrees well with Bai *et al.*'s (2014) data. Several changes are notable under control. The burst frequency $f_b{}^+$ decreases by 17 %, 30 % and 24 % under CUF, GA-I and GA-II, respectively. The corresponding burst strengths, defined as the difference between the maximum and minimum $\langle u^+ \rangle_t$, diminish by 67 %, 80 % and 75 %, and the burst durations contract by 33 %, 37 % and 42 %, respectively. Finally, in three controlled cases, the slopes $\mathrm{d}\langle u^+ \rangle_t / \mathrm{d}t$ in the acceleration stage, directly linked to the sweep motion on the downwash side of the QSVs (Iuso *et al.* 2002), are smaller than in the uncontrolled case, suggesting substantially weakened sweep motions. Consequently, the turbulence regeneration cycle is suppressed, contributing to the DR in TBL. Among the three control strategies, the burst events under GA-I are the weakest, corresponding to the most stable streaks (figure 17) and most pronounced DR (figure 9*a*) at this position.

6.7. *Dissipation and production of the TKE budget*

Variation in the mean energy dissipation and production terms in the TKE budget may provide valuable information for understanding the DR mechanisms. Figure 20 presents time-averaged production and dissipation terms of TKE at $x^+ \approx 33$, when

https://doi.org/10.1017/jfm.2026.11625 Published online by Cambridge University Press

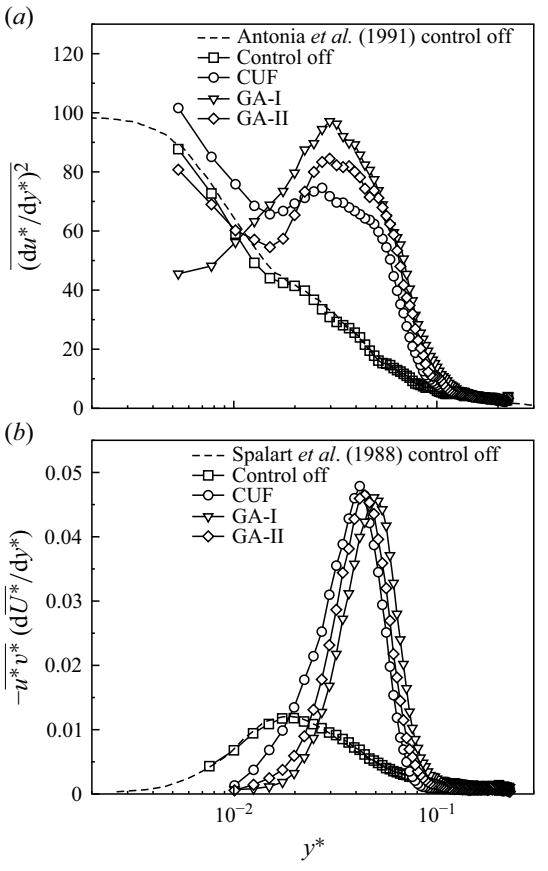


Figure 20. Wall-normal variation of time-averaged (*a*) the predominant component $\overline{(\mathrm{d}u/\mathrm{d}y)^2}$ of the mean TKE dissipation and (*b*) production $-\overline{uv}(\mathrm{d}\overline{U}/\mathrm{d}y)$. The data correspond to P1, P2 and P3 in figure 9*a*. Superscript '$*$' denotes normalization by outer scales.

the maximum DR is obtained. Some remarks are due on the possible effect of the phase shift between the synthetic jets on turbulent statistics. We did perform phase-averaging under GA-I at three representative phases ($t/T = 0.25,\ 0.5,\ 0.75$) and observed that the second-order statistics measured at $x^+ \approx 33$ exhibited little dependence on phase (not shown). The observation may be ascribed to two factors. Firstly, the measurement location at $x^+ \approx 33$ is sufficiently far for adequate turbulent mixing so that the broadband fluctuations of turbulence smear out the phase-locked signatures originating at synthetic jets. Secondly, the spanwise motion generated under GA-I or GA-II enhances the exchanges of perturbations at different phases. Both act to reduce the phase effect on the TKE dissipation and production estimated at $x^+ = 33$. Among the 12 terms of the mean energy dissipation, $\overline{(\mathrm{d}u/\mathrm{d}y)^2}$ accounts for approximately 80 % of the total dissipation in the viscous sublayer and 41 %–72 % in the buffer layer (Antonia, Kim & Browne 1991; Qiao *et al.* 2019). Figure 20(*a*) presents $\overline{(\mathrm{d}u/\mathrm{d}y)^2}$ calculated from the PIV data in the x–y plane. In the absence of control, $\overline{(\mathrm{d}u^*/\mathrm{d}y^*)^2}$ agrees well with Antonia *et al.*'s (1991) DNS data, thus providing a validation for the present estimate of $\overline{(\mathrm{d}u/\mathrm{d}y)^2}$. The $\overline{(\mathrm{d}u^*/\mathrm{d}y^*)^2}$ under CUF is higher than the natural TBL, and a broad peak occurs over $0.018 < y^* < 0.09$, corresponding

https://doi.org/10.1017/jfm.2026.11625 Published online by Cambridge University Press

to $10 < y^+ < 50$. Qiao *et al.* (2018) perturbed the TBL using piezoceramic actuators, which generated small-scale streamwise vortices. They observed a marked rise in $\overline{(\mathrm{d}u/\mathrm{d}y)^2}$ near the wall ($y^+ < 30$). So did Cheng *et al.* (2021*a*) using unsteady blowing through one array of streamwise slits, which again produced small-scale streamwise vortices. These findings suggest that small-scale streamwise vortices can be dissipative, irrespective of the manner of their generation, thus accounting for the occurrence of the broad peak. Under GA-I and GA-II, the spanwise velocity transports more generated streamwise vortices to the measurement location, leading to the more pronounced broad peak in $\overline{(\mathrm{d}u^*/\mathrm{d}y^*)^2}$ than under CUF. This position is different from Cheng *et al.*'s (2021*b*) observation that the maximum spanwise velocity occurred at $y^+ = 20$. This difference is ascribed to the fact that the present spanwise motion is associated with a suction process, which acts to draw the spanwise motion closer to the wall. Choi *et al.* (1994) investigated the influences of the near-wall spanwise velocity on a turbulent channel flow based on the DNS data, and noted a similarly reduced dissipation at $y^+ < 5$, where the randomly occurring streaky structures diminished. Note that the near-wall spanwise motion generated under GA-I is stronger than GA-II, thus accounting for a smaller $\overline{(\mathrm{d}u^*/\mathrm{d}y^*)^2}$, which is internally consistent with the higher local maximum DR (75 %) under GA-I than that (70 %) under GA-II.

The production term $-\overline{u^*v^*}(\mathrm{d}\overline{U^*}/\mathrm{d}y^*)$ agrees well with Spalart's (1988) DNS data in the absence of control (figure 20*b*), lending a support for the present measurement. In natural TBL, the QSV-induced low speed streaks produce strong velocity fluctuations after bursting, which is an important source of TKE. Kim, Kline & Reynolds (1971) demonstrated a strong positive correlation between the TKE production term and the burst events. In the viscous sublayer ($y^+ < 5$ or $y^* < 0.009$), $-\overline{u^*v^*}(\mathrm{d}\overline{U^*}/\mathrm{d}y^*)$ is smaller under all the control schemes than in the absence of control, and varies little from one control scheme to another. In the part of the buffer layer near the wall, $-\overline{u^*v^*}(\mathrm{d}\overline{U^*}/\mathrm{d}y^*)$ remains smaller under control than in the natural TBL. The drop in the production term is due to the weakened burst event and stabilized streaky structures, which have been confirmed in §§ 6.6 and 6.4, respectively. Thus, the turbulent regeneration cycle is inhibited, resulting in the reduced skin friction. Under GA-I, the production at $0.009 < y^* < 0.025$ ($5 < y^+ < 14$) is smallest of all, internally consistent with the least energetic large-scale structures in the buffer layer and viscous sublayer (figures 16, 18 and 19). As noted earlier, the spanwise motion may act to stabilize the streaky structures, accounting for the reduced TKE in the part of buffer layer near the wall. The peaks of $-\overline{u^*v^*}(\mathrm{d}\overline{U^*}/\mathrm{d}y^*)$ occur at $y^* = 0.04$ ($y^+ = 23$), 0.052 ($y^+ = 29$) and 0.046 ($y^+ = 26$) under CUF, GA-I and GA-II, respectively, above that ($y^* = 0.02$ or $y^+ = 11$) in the natural TBL, coinciding with the peaks of u_{rms^*} (figure 16*d*). At $y^+ = 10\sim15$ in natural TBL, the intensity of the burst event is very significant, resulting in a peak in $-\overline{u^*v^*}(\mathrm{d}\overline{U^*}/\mathrm{d}y^*)$ (Blackwelder & Kaplan 1976). Therefore, the upward shift in the peak value of $-\overline{u^*v^*}(\mathrm{d}\overline{U^*}/\mathrm{d}y^*)$ under control indicates that the most likely position of burst events moves away from the wall, along with the lifted streaky structures and QSVs. The lifted coherence structures are also reflected in the u_{rms} profile, as discussed in § 6.3, and the visualized streaky structures noted in § 6.4. The relationship between the upward shift in ${u_{rms}}^*$ or $-\overline{u^*v^*}(\mathrm{d}\overline{U^*}/\mathrm{d}y^*)$ and the lifted coherent structures is also observed by Cheng *et al.* (2021*a*) in their TBL control experiment using unsteady blowing.

6.8. *Phase-averaged DR*

The cyclic modulation of the DR under CUF at $x^+ = 33$ is calculated based on a phase average technique to cast light upon how the different stages of the synthetic jets are

https://doi.org/10.1017/jfm.2026.11625 Published online by Cambridge University Press

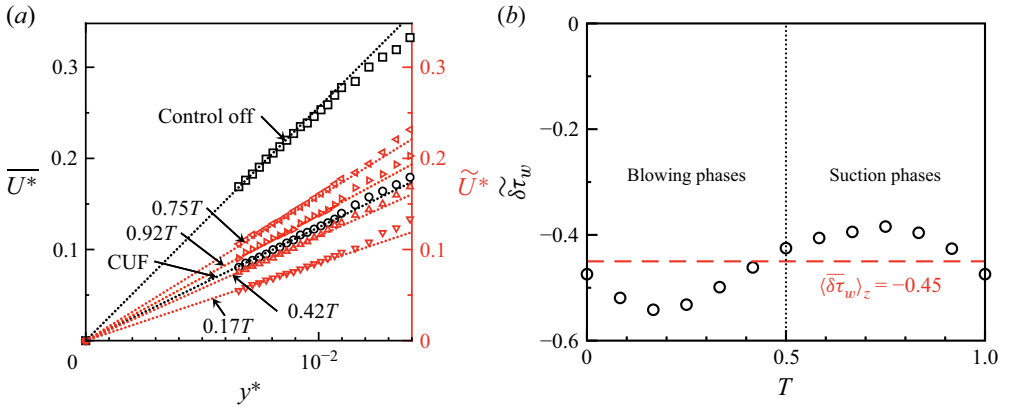


Figure 21. (*a*) Time- and phase-averaged streamwise velocities, distinguished by black and red colours, respectively, under CUF normalized by outer scale. (*b*) Variation of phase-averaged δ_{τ_w}, i.e. $\widetilde{\delta_{\tau_w}}$ at the different phases of CUF actuation.

connected to the drag variation. The nonlinearity of turbulence is reflected in its high randomness over time and space. Statistical quantities, such as mean velocity and TKE, may provide a simplified and generalized understanding of turbulence. In this section, each phase plot is the ensemble average of 180 separate instantaneous events. Further, the phase-averaged data was obtained at $x^+ = 33$, very close to the trailing edge of actuation, where the manipulated flow remains highly correlated to the phases of synthetic jets. Figure 21(*a*) presents the near-wall time-averaged streamwise velocity profiles with and without CUF at $(x^+, z^+) = (33, 0)$. The phase averaged DR $\widetilde{\delta_{\tau_w}}$ ('$\sim$' denotes phase-averaging) within one period, T, of actuation is not constant and may vary with time, which can be obtained from the phase-averaged data, also given in figure 21(*a*). For instance, the slopes of the phase-averaged velocity profile $\widetilde{U^*}$ in the sublayer vary at $t = 0.17T$, $0.42T$, $0.75T$ and $0.92T$ (figure 21*a*), which determine the DR at different phases of one period. As shown in figure 21(*b*), the WSS decreases under blowing or with weakening suction but increases with impairing blowing or under suction. This is not surprising. Steady blowing can increase the thickness of the downstream TBL, thus reducing the velocity gradient within the boundary layer and achieving DR, whilst steady suction does the opposite (Park & Choi 1999; Stroh *et al.* 2016). Tardu (2001) investigated the effect of periodical blowing through a spanwise slot on the near-wall turbulence characteristics. Their phase-averaged WSS indicated a suppressed wall turbulence during the acceleration phase of blowing. A similar observation was also made by Li *et al.* (2023) who deployed three annular synthetic jets for the manipulation of a TBL around a body of revolution. They found that the blowing or suction phase made a positive or negative contribution to the DR.

6.9. *Drag reduction mechanisms*

Based on the previous discussion of various aspects of the flow with and without control, following scenarios are proposed for three controlled cases. Under CUF, the synthetic jets inject ZSM fluid into the near-wall region, which reduces both $\overline{U}$ and $\partial U/\partial y$ within the viscous sublayer, contributing to DR (figure 16). Furthermore, because the blowing intensity overwhelms that of suction (figure 4), the synthetic jets act to push the near-wall QSVs away from the wall, as evidenced by the outward shifted u_{rms} peak from $y^+ = 11$ to $y^+ = 23$ (figure 16). As such, it would be difficult for sweep motions associated with

https://doi.org/10.1017/jfm.2026.11625 Published online by Cambridge University Press

the QSVs to reach the wall, reducing the occurrence of large local WSS. Under GA-I and GA-II, the spanwise motions towards the symmetry plane are generated due to a phase shift between adjacent synthetic jets, accounting for an increase in spanwise-averaged DR by 7 %, measured at $x^+ = 33$ (figure 9). However, the spanwise motions are fundamentally different from the widely known spanwise forcing (e.g. Schoppa & Hussain 1998). The latter targets the buffer layer ($y^+ = 10\sim30$), and the generated maximum spanwise velocity is preferably to occur at $y^+ = 24\sim30$ (Yao *et al.* 2017; Cheng *et al.* 2021*b*). This forcing acts directly on streaks that have already formed and been amplified, reducing their instability and transient-growth gain by weakening or stabilizing them (Yao *et al.* 2017; Duong *et al.* 2021; Cheng *et al.* 2021*b*; Meyers *et al.* 2025). On the other hand, the present spanwise motions induced by synthetic jets take place largely within the viscous sublayer, and the wall-normal distributions of spanwise-averaged $\overline{W^+}$, i.e. $\langle\overline{W}\rangle_z^+$ display their maximum $\langle\overline{W}\rangle_z^+$ at $y^+\approx 5$ (figure 14). This result produces two effects. One is to transport the injected ZSM fluid along the spanwise direction and to accelerate its spanwise spread in the viscous sublayer, which is beneficial to reducing spanwise-averaged U and hence DR. The other is to homogenize the near-wall streamwise velocity distribution (figure 17), reducing $\partial U/\partial z$. In the natural TBL, the low-speed streaks are associated with strong spanwise shear $\partial U/\partial z$ on their flanks, which generates wall-normal vorticity. This vorticity provides disturbance essential to the STG mechanism (Schoppa & Hussain 1998). The STG is essentially the process by which wall normal or spanwise disturbances extract energy from the mean shear through the lift-up effect and amplify streamwise streaks (Brandt 2014). For the near-wall turbulence regeneration cycle, the STG occupies a critical intermediate stage linking 'streamwise-vortex-induced streak formation' to 'streak amplification/instability' and ultimately to the regeneration of near-wall streamwise vortices and therefore serves as an important bridge in the conversion of streaks into new QSVs (Hamilton *et al.* 1995; Schoppa & Hussain 2002; Deng & Xu 2012). Then the reduced $\partial U/\partial z$ under GA-I and GA-II acts to suppress the precursor conditions for the STG, thus inhibiting the formation of the viscous sublayer streaks (figure 17). Note that the viscous sublayer streaks serve as the 'seeds' for streak formation in the overlying buffer layer (Schoppa & Hussain 2002), and suppressing the STG and streaks within this layer interrupts the turbulence regeneration cycle at an early stage, thus contributing to DR. Consequently, the activities associated with near-wall QSVs will be impaired and even suppressed (figure 19), which directly explains two observations, i.e. the more pronounced decrease in ${u_{rms}}^+$ at $y^+ < 11$ under GA-I and GA-II than under CUV (figure 16) and the rather stabilized near-wall flow (figure 20).

It is of relevance to comment on the effectiveness of GA-I or GA-II at high Reynolds numbers. As demonstrated by Cheng *et al.* (2021*a*), the first and second DR mechanisms mentioned above play dominant and minor roles, accounting for 77 % and 23 % of DR, respectively, when one array of periodic blowing jets is deployed. The former is further confirmed to work even at $Re_\tau = 18\ 000$ when Zhang *et al.* (2024) deployed steady blowing, which achieved a spatially averaged DR beyond 70 %. However, the effectiveness of this mechanism could be adversely affected by the gap between the synthetic jets, which could be too big for very high Re_τ. On the other hand, whether the spanwise motion can be effective in achieving DR at high Reynolds numbers lies in whether this motion can cover the viscous sublayer. Yao *et al.* (2017) showed that, as Re_τ increased from 104 to 550, the failure of large-scale swirl control in Canton *et al.* (2016*b*) was not due to flaws in the large-scale manipulation concept, but rather the inability of the control flow to influence sufficiently the viscous sublayer and thereby intervene in STG. As Re_τ increases, the viscous sublayer becomes thinner in physical units, and a control flow centred far from

https://doi.org/10.1017/jfm.2026.11625 Published online by Cambridge University Press

the wall can no longer effectively influence the near-wall region. The synthetic-jet array developed presently produces a spanwise motion that is confined to the near wall region. As shown in figure 14, the maximum time-averaged spanwise velocity occurs at $y^+ = 5$ under both GA-I and GA-II ($Re_\tau = 572$). This is within the viscous sublayer and is one order of magnitude closer to the wall than the control flows used in typical large scale manipulation studies, e.g. $y^+ \approx 30$ in Yao *et al.* (2017). As pointed out by Yu *et al.* (2025), the spanwise motions near the wall are not coincidental but an inherent feature when there is a phase difference between adjacent high Strouhal number synthetic jets. Since the suction phase of the synthetic jet pulls the counter-rotating vortices and the associated spanwise motions towards the wall, anchoring them on or near the wall, the spanwise motions, which are part of the control flow, are always attached or very close to the wall. Therefore, it may be speculated that the spanwise motions may still achieve DR at high Re_τ given an adequate strength of synthetic jets.

6.10. *Drag reduction efficiency*

The control efficiency may be defined by $\eta = P_{saved}/P_{used}$, where P_{saved} and P_{used} are the power saved due to DR and power consumed in the control process, respectively. All control strategies shown in figure 7, including CUF, GA-I and GA-II, employ identical voltage and frequency, implying the same energy consumption. Assuming all electrical energy is converted to fluid energy, and the energy loss due to narrow flow passages are neglected, P_{used} can be estimated by $P_{used} = (N/T)\int_0^T\int_0^{L_x}\int_0^{L_z}|\rho(U_{jet}^3/2)|\mathrm{d}z\mathrm{d}x\mathrm{d}t$, where L_x and L_z are the length and width of the slits, respectively. The distribution of the jet exit velocity U_{jet} along the cross-section or z-direction of the slits can be obtained from the PIV data in § 6.1. Due to the large length-to-width ratio (24) of the slits, U_{jet} may be considered to be uniform along the x-direction. Thus, P_{used} may be calculated to be approximately 2.9×10^{-5} W for CUF, GA-I and GA-II. Based on the data in figures 9 and 10, P_{saved} may be calculated by $P_{saved} = \rho u_\tau^2 U_\infty \int_{z_1}^{z_2}\int_{x_1}^{x_2}\overline{\delta_{\tau_w}}\mathrm{d}x\mathrm{d}z$, resulting in 1.24×10^{-5} W, 1.50×10^{-5} W and 1.37×10^{-5} W for CUF, GA-I and GA-II, respectively, and the corresponding efficiencies η are then 0.42, 0.52 and 0.47, respectively. In the DNS of a turbulent channel flow, manipulated using unsteady jets through one array of longitudinal slits, Xi *et al.* (2024) found that DR took place not only in the control region but also upstream and downstream of the control jets. It can be readily found out from a longitudinal integration of local DR that the three regions accounted for 34.2 %, 11.5 % and 54.3 % of the total DR, respectively. In the present work, the blowing stage of the synthetic jet is largely responsible for DR (Ye *et al.* 2019; Li *et al.* 2023). Assume DR takes place upstream and downstream of the synthetic jets as well and the corresponding DR percentages are similar to Xi *et al.*'s (2024) finding. As such, we may estimate the total DRs of CUF, GA-I and GA-II from the three regions, which leads to $\eta = 0.79$, 0.96 and 0.88 for CUF, GA-I and GA-II, respectively. Apparently, the control strategies uncovered from GA enhance appreciably the control efficiency. It is worth mentioning that the present control focuses on one objective, i.e. DR. With the introduction of multiple objective optimization say based on the hummingbird algorithm, the control efficiency can be added as one more objective and then be greatly enhanced, as demonstrated by Chang *et al.* (2025).

7. Conclusions

A data-driven optimization system is developed to control a TBL, which consists of a sensing unit (9 wall-wires), a novel actuation/execution unit and a GA-based control or

https://doi.org/10.1017/jfm.2026.11625 Published online by Cambridge University Press

'thinking' unit, other than the control plant (TBL). The following conclusions can be drawn out of this work.

(i) The presently developed actuation technique is based on one spanwise array of 11 independently operated synthetic jets through longitudinally arranged miniature slits, each jet driven by a piezoceramic membrane. This technique has been found to perform very well. Under CUF, which serves as a reference for the optimization, the maximum local DR may reach 55 % at $(U^+_{jet,max}, f^+) = (4, 0.71)$ and the corresponding spanwise-averaged DR is 45 %, with a reasonably good spanwise uniformity. Furthermore, there is a substantial DR downstream, persisting 500 wall units; the observation suggests a substantial DR over the control area Xi *et al.* (2024). All these performance indicators exceed their counterparts of one array of piezoceramic actuators proposed by Bai *et al.* (2014).

(ii) It has been found that the GA optimized control strategies outperform greatly CUF. The strategies are investigated in the optimization of the 10 independent control parameters, i.e. the phase of each individual jet, of the GA control system. The learning process discovers first one individual that produces the best performed CUF and then two individuals, i.e. GA-I and -II, and finally converges to $J \approx 0.57$, corresponding to a more pronounced DR, after 11 hours of searching or testing for 1000 individual control laws. Compared with CUF, the maximum local DR increases from 55 % to 75 % at $x^+ = 33$, and the spanwise-averaged DR rises from 45 % to 52 %. Furthermore, the DR region downstream of actuation grows from 500 wall units to 650 wall units.

(iii) The proximity maps of representative generations provide an overall picture on the control landscape of individuals. The randomly distributed feature vectors at $n = 1$ evolve gradually and occur largely in three distinct regions with increasing n, each associated with one representative control law, i.e. CUF, GA-I and GA-II. All measurements (hot-wire and flow visualization data) point to the fact that both GA-I and GA-II exhibit superior performances to CUF and GA-I performs even better than GA-II. The feature coordinate γ_1 is found to be correlated strongly with the averaged phase shifts, and CUF is characterized by the smallest γ_1. While the feature coordinate γ_2 is related to the symmetry of individuals. The determined phases of GA-I and GA-II are given as

$$\boldsymbol{\phi_i}^{\boldsymbol{I}} = (0, 0.1\pi, 0.2\pi, 0.3\pi, 0.4\pi, 0.5\pi, 0.4\pi, 0.3\pi, 0.2\pi, 0.1\pi, 0), \tag{7.1a}$$

$$\boldsymbol{\phi_i}^{\boldsymbol{II}} = (0, 0.5\pi, 0.5\pi, 0.5\pi, 0.5\pi, 0.5\pi, 0.5\pi, 0.5\pi, 0.5\pi, 0.5\pi, 0). \tag{7.1b}$$

The well-reported travelling waves (e.g. Du & Karniadakis 2000; Bai *et al.* 2014) are also discernible from an analysis of the phases associated with individual control laws (figure 13). However, it seems plausible that the control laws associated with the travelling waves fail to outperform GA-I or GA-II. As a matter of fact, GA-I may be considered to be one of the variants of the travelling wave, which consists of two travelling waves with opposite-signed phase shifts. The difference in their control performances is linked to the control mechanisms behind.

(iv) The mechanisms are unveiled behind the three typical control schemes. Under CUF, DR arises from several reasons. Firstly, the suction process absorbs near-wall fluid, including streaky structures, QSVs, into the chamber, and then the blowing process injects ZSM fluid into the near-wall flow, reducing near-wall streamwise velocity. Secondly, the QSVs are pushed away from the wall, making it difficult for associated sweep motions to reach the wall. Thus, the turbulence regeneration

https://doi.org/10.1017/jfm.2026.11625 Published online by Cambridge University Press

cycle is interrupted, reducing the production of TKE near the wall and achieving DR. Under GA-I and GA-II, the phase shift between adjacent synthetic jets induces spanwise motions largely within the viscous sublayer, which enhance the spanwise spread of the injected ZSM fluid and homogenize the near-wall streamwise velocity distribution, thus reducing $\partial U/\partial z$ and hence suppressing the precursor conditions for the STG and the formation of the viscous sublayer streaks. Since the 'seeds' for streak formation in the overlying buffer layer are eliminated, the turbulence regeneration cycle is interrupted at an early stage, thus contributing to DR. This is fundamentally different from the previously reported spanwise forcing that works on suppressing the amplification and instability of already developed streaks in the buffer layer.

Acknowledgements. Y.Z. wishes to acknowledge support given to him from NSFC through grants U24B2005 and U25A6006 and from NSF of Zhejiang Province through grant LZ25A020002. Dr D. Fan's contribution towards building the AI control system is greatly appreciated.

Declaration of interest. The authors have no conflict to disclose.

References

ABBASSI, M.R., BAARS, W.J., HUTCHINS, N. & MARUSIC, I. 2017 Skin-friction drag reduction in a high-Reynolds-number turbulent boundary layer via real-time control of large-scale structures. *Intl J. Heat Fluid Flow* **67**, 30–41.

ALAMÉ, K. & MAHESH, K. 2019 Wall-bounded flow over a realistically rough superhydrophobic surface. *J. Fluid Mech.* **873**, 977–1019.

ANTONIA, R., KIM, J. & BROWNE, L. 1991 Some characteristics of small-scale turbulence in a turbulent duct flow. *J. Fluid Mech.* **233**, 369–388.

ANTONIA, R.A., ZHU, Y. & SOKOLOV, M. 1995 Effect of concentrated wall suction on a turbulent boundary layer. *Phys. Fluids* **7** (10), 2465–2474.

BAI, H.L., ZHOU, Y., ZHANG, W.G. & ANTONIA, R.A. 2018 Streamwise vortices and velocity streaks in a locally drag-reduced turbulent boundary layer. *Flow Turbul. Combust.* **100** (2), 391–416.

BAI, H.L., ZHOU, Y., ZHANG, W.G., XU, S.J., WANG, Y. & ANTONIA, R.A. 2014 Active control of a turbulent boundary layer based on local surface perturbation. *J. Fluid Mech.* **750**, 316–354.

BENARD, N., PONS-PRATS, J., PERIAUX, J., BUGEDA, G., BRAUD, P., BONNET, J.P. & MOREAU, E. 2016 Turbulent separated shear flow control by surface plasma actuator: experimental optimization by genetic algorithm approach. *Exp. Fluids* **57** (2), 22.

BLACKWELDER, R.F. & HARITONIDIS, J.H. 1983 Scaling of the bursting frequency in turbulent boundary layers. *J. Fluid Mech.* **132**, 87–103.

BLACKWELDER, R.F. & KAPLAN, R.E. 1976 On the wall structure of the turbulent boundary layer. *J. Fluid Mech.* **76** (1), 89–112.

BRANDT, L. 2014 The lift-up effect: the linear mechanism behind transition and turbulence in shear flows. *Eur. J. Mech. B* **47**, 80–96.

BRUNTON, S.L. & NOACK, B.R.2015 Closed-loop turbulence control: progress and challenges. *Appl. Mech. Rev.* **67** (5), 050801.

CANTON, J., ÖRLÜ, R., CHIN, C., HUTCHINS, N., MONTY, J. & SCHLATTER, P. 2016*a* On large-scale friction control in turbulent wall flow in low Reynolds number channels. *Flow Turbul. Combust.* **97** (3), 811–827.

CANTON, J., ÖRLÜ, R., CHIN, C. & SCHLATTER, P. 2016*b* Reynolds number dependence of large-scale friction control in turbulent channel flow. *Phys. Rev. Fluids* **1** (8), 081501.

CHANG, G.H., TANG, S.L., FAN, D.W. & ZHOU, Y. 2025 AI-based active flow control for drag reduction of a maglev train model. In *Proceedings of 6th International Conference in Numerical and Experimental Aerodynamics of Road Vehicles and Trains (Aerovehicles 6)*, July 1–3, 2025, pp. 59–62. University of Birmingham.

CHECCO, A., OCKO, B.M., RAHMAN, A., BLACK, C.T., TASINKEVYCH, M., GIACOMELLO, A. & DIETRICH, S. 2014 Collapse and reversibility of the superhydrophobic state on nanotextured surfaces. *Phys. Rev. Lett.* **112** (21), 216101.

CHENG, X.Q., QIAO, Z.X., ZHANG, X., QUADRIO, M. & ZHOU, Y. 2021*a* Skin-friction reduction using periodic blowing through streamwise slits. *J. Fluid Mech.* **920**, A50.

https://doi.org/10.1017/jfm.2026.11625 Published online by Cambridge University Press

CHENG, X.Q., WONG, C.W., HUSSAIN, F., SCHRÖDER, W. & ZHOU, Y. 2021*b* Flat plate drag reduction using plasma-generated streamwise vortices. *J. Fluid Mech.* **918**, A24.

CHOI, H., MOIN, P. & KIM, J. 1993 Direct numerical simulation of turbulent flow over riblets. *J. Fluid Mech.* **255**, 503–539.

CHOI, H., MOIN, P. & KIM, J. 1994 Active turbulence control for drag reduction in wall-bounded flows. *J. Fluid Mech.* **262**, 75–110.

CHOI, K.-S. 1989 Near-wall structure of a turbulent boundary layer with riblets. *J. Fluid Mech.* **208**, 417–458.

CHOI, K.-S. & CLAYTON, B.R. 2001 The mechanism of turbulent drag reduction with wall oscillation. *Intl J. Heat Fluid Flow* **22** (1), 1–9.

CHOI, K.-S., YANG, X., CLAYTON, B., GLOVER, E., ATLAR, M., SEMENOV, B. & KULIK, V. 1997 Turbulent drag reduction using compliant surfaces. *Proc. R. Soc. Lond. A* **453** (1965), 2229–2240.

CORKE, T.C. & THOMAS, F.O. 2018 Active and passive turbulent boundary-layer drag reduction. *AIAA J.* **56** (10), 3835–3847.

COX, T.F. & COX, M.A.A. 2000 Multidimensional scaling. In *Monographs On Statistics and Applied Probability*, vol. 88. Chapman and Hall.

DANIELLO, R.J., WATERHOUSE, N.E. & ROTHSTEIN, J.P. 2009 Drag reduction in turbulent flows over superhydrophobic surfaces. *Phys. Fluids* **21** (8), 085103.

DEBIEN, A., VON KRBEK, K.A.F.F., MAZELLIER, N., DURIEZ, T., CORDIER, L., NOACK, B.R., ABEL, M.W. & KOURTA, A. 2016 Closed-loop separation control over a sharp edge ramp using genetic programming. *Exp. Fluids* **57** (3), 40.

DELAUNAY, B. 1934 Sur la sphère vide. A la mémoire de Georges Voronoï. *Cl. Sci. Math. Nat.* **6**, 793–800.

DENG, B.Q. & XU, C.X. 2012 Influence of active control on STG-based generation of streamwise vortices in near-wall turbulence. *J. Fluid Mech.* **710**, 234–259.

DI CICCA, G.M., IUSO, G., SPAZZINI, P.G. & ONORATO, M. 2002 Particle image velocimetry investigation of a turbulent boundary layer manipulated by spanwise wall oscillations. *J. Fluid Mech.* **467**, 41–56.

DU, Y. & KARNIADAKIS, G.E. 2000 Suppressing wall turbulence by means of a transverse travelling wave. *Science* **288**, 1230–1234.

DUONG, A.H., CORKE, T.C. & THOMAS, F.O. 2021 Characteristics of drag-reduced turbulent boundary layers with pulsed-direct-current plasma actuation. *J. Fluid Mech.* **915**, A113.

DURIEZ, T., BRUNTON, S.L. & NOACK, B.R. 2017 *Machine Learning Control: Taming Nonlinear Dynamics and Turbulence*, Fluid Mechanics and its Applications, vol. 116. Springer-Verlag.

ENDO, T., KASAGI, N. & SUZUKI, Y. 2000 Feedback control of wall turbulence with wall deformation. *Intl J. Heat Fluid Flow* **21** (5), 568–575.

FAN, D., ZHANG, B., ZHOU, Y. & NOACK, B.R. 2020*a* Optimization and sensitivity analysis of active drag reduction of a square-back Ahmed body using machine learning control. *Phys. Fluids* **32** (12), 125117.

FAN, D., ZHOU, Y. & NOACK, B.R. 2020*b* Fast triple-parameter extremum seeking exemplified for jet control. *Exp. Fluids* **61** (7), 152.

FUKAGATA, K., KERN, S., CHATELAIN, P., KOUMOUTSAKOS, P. & KASAGI, N. 2008 Evolutionary optimization of an anisotropic compliant surface for turbulent friction drag reduction. *J. Turbul.* **9**, N35.

GAUTIER, N., AIDER, J.L., DURIEZ, T., NOACK, B.R., SEGOND, M. & ABEL, M. 2015 Closed-loop separation control using machine learning. *J. Fluid Mech.* **770**, 442–457.

GOLDBERG, D.E. 1989 *Genetic Algorithms in Search, Optimization, and Machine Learning*. Addison-Wesley Pub. Co.

HAMILTON, J.M., KIM, J. & WALEFFE, F. 1995 Regeneration mechanisms of near-wall turbulence structures. *J. Fluid Mech.* **287**, 317–348.

HUSSAIN, A.F. 1986 Coherent structures and turbulence. *J. Fluid Mech.* **173**, 303–356.

HUTCHINS, N. & CHOI, K.-S. 2002 Accurate measurements of local skin friction coefficient using hot-wire anemometry. *Prog. Aerosp. Sci.* **38**, 421–446.

ITOH, M., TAMANO, S., YOKOTA, K. & TANIGUCHI, S. 2006 Drag reduction in a turbulent boundary layer on a flexible sheet undergoing a spanwise traveling wave motion. *J. Turbul.* **7** (27), N27.

IUSO, G., DI CICCA, G.M., ONORATO, M., SPAZZINI, P.G. & MALVANO, R. 2003 Velocity streak structure modifications induced by flow manipulation. *Phys. Fluids* **15** (9), 2602–2612.

IUSO, G., ONORATO, M., SPAZZINI, P.G. & DI CICCA, G.M. 2002 Wall turbulence manipulation by large-scale streamwise vortices. *J. Fluid Mech.* **473**, 23–58.

JACOBSON, S.A. & REYNOLDS, W.C. 1998 Active control of streamwise vortices and streaks in boundary layers. *J. Fluid Mech.* **360**, 179–211.

JEONG, J., HUSSAIN, F., SCHOPPA, W. & KIM, J. 1997 Coherent structures near the wall in a turbulent channel flow. *J. Fluid Mech.* **332**, 185–214.

https://doi.org/10.1017/jfm.2026.11625 Published online by Cambridge University Press

JOHANSSON, A.V., ALFREDSSON, P.H. & KIM, J. 1991 Evolution and dynamics of shear-layer structures in near-wall turbulence. *J. Fluid Mech.* **224**, 579–599.
JUNG, W.J., MANGIAVACCHI, N. & AKHAVAN, R. 1992 Suppression of turbulence in wall-bounded flows by high-frequency spanwise oscillations. *Phys. Fluids A* **4** (8), 1605–1607.
KAMETANI, Y. & FUKAGATA, K. 2011 Direct numerical simulation of spatially developing turbulent boundary layers with uniform blowing or suction. *J. Fluid Mech.* **681**, 154–172.
KANG, S. & CHOI, H. 2000 Active wall motions for skin-friction drag reduction. *Phys. Fluids* **12** (12), 3301–3304.
KIM, H.T., KLINE, S.J. & REYNOLDS, W.C. 1971 The production of turbulence near a smooth wall in a turbulent boundary layer. *J. Fluid Mech.* **50** (1), 133–160.
KIM, J. 1983 On the structure of wall-bounded turbulent flows. *Phys. Fluids* **26** (8), 2088–2097.
KIM, J., KIM, K. & SUNG, H.J. 2003 Wall pressure fluctuations in a turbulent boundary layer after blowing or suction. *AIAA J.* **41** (9), 1697–1704.
KIM, K. & SUNG, H.J. 2006 Effects of unsteady blowing through a spanwise slot on a turbulent boundary layer. *J. Fluid Mech.* **557**, 423–450.
KLINE, S.J., REYNOLDS, W.C., SCHRAUB, F.A. & RUNSTADLER, P.W. 1967 The structure of turbulent boundary layers. *J. Fluid Mech.* **30** (4), 741–773.
KRAVCHENKO, A.G., CHOI, H. & MOIN, P. 1993 On the relation of near-wall streamwise vortices to wall skin friction in turbulent boundary layers. *Phys. Fluids A* **5** (12), 3307–3309.
LAI, P., WANG, R., ZHANG, W. & XU, H. 2021 Parameter optimization of open-loop control of a circular cylinder by simplified reinforcement learning. *Phys. Fluids* **33**, 107110.
LEE, T., FISHER, M. & SCHWARZ, W. 1993 Investigation of the stable interaction of a passive compliant surface with a turbulent boundary layer. *J. Fluid Mech.* **257**, 373–401.
LI, H., YU, J., CHEN, Z. & REN, K. 2023 Numerical research on drag-reduction characteristics of a body of revolution based on periodic forcing. *Ocean Engng* **280**, 114909.
LI, R.Y., NOACK, B.R., CORDIER, L., BORÉE, J. & HARAMBAT, F. 2017 Drag reduction of a car model by linear genetic programming control. *Exp. Fluids* **58**, 1–20.
LI, W., ROGGENKAMP, D., HECKEN, T., JESSEN, W., KLAAS, M. & SCHRÖDER, W. 2018 Parametric investigation of friction drag reduction in turbulent flow over a flexible wall undergoing spanwise transversal traveling waves. *Exp. Fluids* **59** (6), 105.
LI, Y., CUI, W., JIA, Q., LI, Q., YANG, Z., MORZYŃSKI, M. & NOACK, B.R. 2022 Explorative gradient method for active drag reduction of the fluidic pinball and slanted Ahmed body. *J. Fluid Mech.* **932**, A7.
LOU, Y., SUN, S. & NOCEDAL, J. 2025 Design guidelines for noise-tolerant optimization with applications in robust design. *SIAM J. Sci. Comput.* **47** (3), A1335–A1357.
LU, L., LI, D., GAO, Z., CAO, Z., BAI, Y. & ZHENG, J. 2020 Characteristics of array of distributed synthetic jets and effect on turbulent boundary layer. *Acta Mechanica Sin.* **36** (6), 1171–1190.
MARTELL, M.B., PEROT, J.B. & ROTHSTEIN, J.P. 2009 Direct numerical simulations of turbulent flows over superhydrophobic surfaces. *J. Fluid Mech.* **620**, 31–41.
MEYERS, A., DUONG, A., CORKE, T.C. & THOMAS, F.O. 2025 Characterizing turbulent boundary layer response and recovery to buffer region spanwise blowing. *J. Fluid Mech.* **1016**, A26.
MINELLI, G., DONG, T., NOACK, B.R. & KRAJNOVIĆ, S. 2020 Upstream actuation for bluff-body wake control driven by a genetically inspired optimization. *J. Fluid Mech.* **893**, A1.
MITO, Y. & KASAGI, N. 1998 DNS study of turbulence modification with streamwise-uniform sinusoidal wall-oscillation. *Intl J. Heat Fluid Flow* **19** (5), 470–481.
NABAE, Y., KAWAI, K. & FUKAGATA, K. 2020 Prediction of drag reduction effect by streamwise traveling wave-like wall deformation in turbulent channel flow at practically high Reynolds numbers. *Intl J. Heat Fluid Flow* **82**, 108550.
NAKANISHI, R., MAMORI, H. & FUKAGATA, K. 2012 Relaminarization of turbulent channel flow using traveling wave-like wall deformation. *Intl J. Heat Fluid Flow* **35**, 152–159.
ORLANDI, P. & JIMÉNEZ, J. 1994 On the generation of turbulent wall friction. *Phys. Fluids* **6** (2), 634–641.
PARIS, R., BENEDDINE, S. & DANDOIS, J. 2021 Robust flow control and optimal sensor placement using deep reinforcement learning. *J. Fluid Mech.* **913**, A25.
PARK, J. & CHOI, H. 1999 Effects of uniform blowing or suction from a spanwise slot on a turbulent boundary layer flow. *Phys. Fluids* **11** (10), 3095–3105.
PIROZZOLI, S. & SMITS, A.J. 2023 Outer-layer universality of the mean velocity profile in turbulent wall-bounded flows. *Phys. Rev. Fluids* **8** (6), 064607.
QAYOUM, A., GUPTA, V., PANIGRAHI, P.K. & MURALIDHAR, K. 2010 Perturbation of a laminar boundary layer by a synthetic jet for heat transfer enhancement. *Intl J. Heat Mass Transfer* **53** (23–24), 5035–5057.

https://doi.org/10.1017/jfm.2026.11625 Published online by Cambridge University Press

QIAO, Z.X., MINELLI, G., NOACK, B.R., KRAJNOVIĆ, S. & CHERNORAY, V. 2021 Multi-frequency aerodynamic control of a yawed bluff body optimized with a genetic algorithm. *J. Wind Engng Ind. Aerodyn.* **212**, 104600.

QIAO, Z.X., WU, Z. & ZHOU, Y. 2018 Turbulent boundary layer manipulation under a proportional-derivative closed-loop scheme. *Phys. Fluids* **30**, 115101.

QIAO, Z.X., XU, S.J. & ZHOU, Y. 2019 On the measurement of wall-normal velocity derivative in a turbulent boundary layer. *Flow Turbul. Combust.* **103** (2), 369–387.

QIAO, Z.X., ZHOU, Y. & WU, Z. 2017 Turbulent boundary layer under the control of different schemes. *Proc. Math. Phys. Sci.* **473**, 20170038.

QUADRIO, M. 2011 Drag reduction in turbulent boundary layers by in-plane wall motion. *Phil. Trans. A Math. Phys. Engng Sci.* **369**, 1428–1442.

QUADRIO, M. & LUCHINI, P. 2003 Integral space–time scales in turbulent wall flows. *Phys. Fluids* **15** (8), 2219–2227.

QUADRIO, M. & RICCO, P. 2004 Critical assessment of turbulent drag reduction through spanwise wall oscillations. *J. Fluid Mech.* **521**, 251–271.

QUADRIO, M., RICCO, P. & VIOTTI, C. 2009 Streamwise-travelling waves of spanwise wall velocity for turbulent drag reduction. *J. Fluid Mech.* **627**, 161–178.

RABAULT, J., KUCHTA, M., JENSEN, A., RÉGLADE, U. & CERARDI, N. 2019 Artificial neural networks trained through deep reinforcement learning discover control strategies for active flow control. *J. Fluid Mech.* **865**, 281–302.

RASTEGARI, A. & AKHAVAN, R. 2018 The common mechanism of turbulent skin-friction drag reduction with superhydrophobic longitudinal microgrooves and riblets. *J. Fluid Mech.* **838**, 68–104.

RATHNASINGHAM, R. & BREUER, K.S. 2003 Active control of turbulent boundary layers. *J. Fluid Mech.* **495**, 209–233.

ROBINSON, S. 1991 Coherent motions in the turbulent boundary layer. *Annu. Rev. Fluid Mech.* **23** (1), 601–639.

ROBINSON, S.K. 1990 A review of vortex structures and associated coherent motions in turbulent boundary layers. In *Structure of Turbulence and Drag Reduction: IUTAM Symposium*, July 25–28, Zurich, pp. 23–50. Springer.

SCHOPPA, W. & HUSSAIN, F. 1998 A large-scale control strategy for drag reduction in turbulent boundary layers. *Phys. Fluids* **10** (5), 1049–1051.

SCHOPPA, W. & HUSSAIN, F. 2002 Coherent structure generation in near-wall turbulence. *J. Fluid Mech.* **453**, 57–108.

SKOTE, M. 2011 Turbulent boundary layer flow subject to streamwise oscillation of spanwise wall-velocity. *Phys. Fluids* **23**, 081703.

SMITH, C. 1984 A Synthesized Model of the Near-Wall Behavior in Turbulent Boundary Layers. In *Proceedings of the 8th Symposium on Turbulence,* pp. 299–325. University Missouri-Rolla.

SPALART, P.R. 1988 Direct simulation of a turbulent boundary layer up to Rθ = 1410. *J. Fluid Mech.* **187**, 61–98.

SPINOSA, E. & ZHONG, S. 2017 Reduction of Skin Friction Drag in a Turbulent Boundary Layer Using Circular Synthetic Jets. In *55th AIAA Aerospace Sciences Meeting, 9–13 January 2017, Grapevine, Texas*.

STROH, A., HASEGAWA, Y., SCHLATTER, P. & FROHNAPFEL, B. 2016 Global effect of local skin friction drag reduction in spatially developing turbulent boundary layer. *J. Fluid Mech.* **805**, 303–321.

TANG, H., RABAULT, J., KUHNLE, A., WANG, Y. & WANG, T. 2020 Robust active flow control over a range of Reynolds numbers using an artificial neural network trained through deep reinforcement learning. *Phys. Fluids* **32** (5), 053605.

TARDU, S.F. 2001 Active control of near-wall turbulence by local oscillating blowing. *J. Fluid Mech.* **439**, 217–253.

THOMAS, F.O., CORKE, T.C., DUONG, A., MIDYA, S. & YATES, K. 2019 Turbulent drag reduction using pulsed-DC plasma actuation. *J. Phys. D: Appl. Phys.* **52** (43), 434001.

TOMIYAMA, N. & FUKAGATA, K. 2013 Direct numerical simulation of drag reduction in a turbulent channel flow using spanwise traveling wave-like wall deformation. *Phys. Fluids* **25** (10), 105115.

UTTURKAR, Y., ARIK, M., SEELEY, C.E. & GURSOY, M. 2008 An experimental and computational heat transfer study of pulsating jets. *J. Heat Transfer* **130**, 062201.

WALSH, M.J. 1983 Riblets as a viscous drag reduction technique. *AIAA J.* **21** (4), 485–486.

WEI, X. & ZHOU, Y. 2024 Scaling of drag reduction in a turbulent boundary layer based on plasma-generated streamwise vortices. In *Proceedings of 13th International Symposium on Turbulence and Shear Flow Phenomena*, 25–38 Jun 2024, Montreal, Canada. Paper no. 389.

WEI, X. & ZHOU, Y. 2025 Scaling of flat plate drag reduction using plasma-generated streamwise vortices. *J. Fluid Mech.* **1007**, R5.

https://doi.org/10.1017/jfm.2026.11625 Published online by Cambridge University Press

WONG, C.W., ZHOU, Y., LI, Y. & LI, Y. 2015 Active drag reduction in a turbulent boundary layer based on plasma-actuator-generated streamwise vortices. In *Proceeding of the 9th International Symposium on Turbulence and Shear Flow Phenomena*, June 30 – July 3 2015, The University of Melbourne, Australia. Paper no. 209.

WU, Z., WONG, C.W. & ZHOU, Y. 2018 Dual-input/Single-output extremum-seeking system for jet control. *AIAA J.* **56** (4), 1463–1471.

XI, L., QUADRIO, M. & ZHOU, Y. 2024 Direct numerical simulation of skin-friction reduction using steady and periodic blowing through streamwise slits. In *Fluid-Structure-Sound Interactions and Control*, pp. 85–90.

YAO, J., CHEN, X. & HUSSAIN, F. 2018 Drag control in wall-bounded turbulent flows via spanwise opposed wall-jet forcing. *J. Fluid Mech.* **852**, 678–709.

YAO, J., CHEN, X., THOMAS, F. & HUSSAIN, F. 2017 Large-scale control strategy for drag reduction in turbulent channel flows. *Phys. Rev. Fluids* **2** (6), 062601.

YE, Z., JIANG, Y., ZHANG, Y., ZOU, J. & ZHENG, Y. 2019 Effects of synthetic jet array on turbulent boundary layer. *Intl J. Heat Technol.* **37** (3), 893–898.

YU, J., FAN, D., NOACK, B.R. & ZHOU, Y. 2022 Genetic-algorithm-based artificial intelligence control of a turbulent boundary layer. *Acta Mechanica Sin.* **37** (12), 1739–1747.

YU, J., MI, J. & ZHOU, Y. 2025 Interactions between adjacent synthetic-jet-generated vortices of high Strouhal number. *Phys. Fluids* **37** (9), 097112.

ZHANG, B., FAN, D. & ZHOU, Y. 2023 Artificial intelligence control of a low-drag Ahmed body using distributed jet arrays. *J. Fluid Mech.* **963**, A3.

ZHANG, K., LUO, J., WEI, X. & ZHOU, Y. 2023 Skin Friction Reduction in a Turbulent Boundary Layer with Miniature Vortex Generators, Busan. In *6th Symposium on Fluid-Structure-Sound Interactions and Control, August 26–30, 2023, Busan, Korea*, pp. 39–45. Springer.

ZHANG, X., WEI, X.H., WANG, H.F. & ZHOU, Y. 2024 Skin Friction Reduction in a High Reynolds Number Turbulent Boundary Layer Using Spanwise Blowing Microjets. In *Fluid-Structure-Sound Interactions and Control. FSSIC 2023*. Springer.

ZHOU, Y., FAN, D., ZHANG, B., LI, R. & NOACK, B.R. 2020 Artificial intelligence control of a turbulent jet. *J. Fluid Mech.* **897**, A27.

ZIGUNOV, F., SELLAPPAN, P. & ALVI, F. 2021 Beyond actuator line arrays in active flow control studies: lessons from a genetic algorithm approach. *Phys. Rev. Fluids* **6** (8), 083903.

https://doi.org/10.1017/jfm.2026.11625 Published online by Cambridge University Press